remote sensing

MDPI

Article

Whittle–Matérn Roughness Covariance for C-Band SAR Inversion over Bare Agricultural Soil

Yiqi Wang [1] and Yang Du [1,2,*]

[1] College of Information Science and Electronic Engineering, Zhejiang University, Hangzhou 310027, China; 12531016@zju.edu.cn
[2] Innovation Center of Yangtze River Delta, Zhejiang University, Jiashan 314102, China
* Correspondence: zjuydu03@zju.edu.cn

Highlights

What are the main findings?

- Rough surface covariance structure materially affects the attainable co-polarized backscatter domain in unregularized multi-sensor SAR inversion over bare agricultural soil.
- The Whittle–Matérn (WM) model, interpreted as a Gaussian–Gamma scale mixture, represents multiscale roughness and yields the lowest blind point ratio (3.19%) and the lowest reconstruction error in four of the five SAR channels.

What are the implications of the main findings?

- Covariance misspecification can propagate into compensatory changes in retrieved roughness and soil moisture parameters, affecting both inversion feasibility and the physical interpretation of the retrieved variables.
- Multiscale covariance models such as WM expand the attainable backscatter domain and improve scene scale consistency of soil moisture retrievals, subject to independent pixel scale validation.

Abstract

This study evaluates whether the Whittle–Matérn (WM) covariance representation improves pixel-wise SAR inversion over bare agricultural soil which can exhibit scale-dependent roughness. WM includes a smoothness parameter that controls covariance and roughness spectrum shape and has a Gaussian–Gamma scale-mixture interpretation. It was compared with exponential, Gaussian, and powered exponential (PE) covariance models within the same modified extended advanced integral equation model. Co-registered RADARSAT-2 and Sentinel-1 observations provided five channels for inversion. All experiments used identical observations, ancillary inputs, parameter bounds, objective function, and multi-start optimization settings. The analysis focused on the three co-polarized channels, for which covariance structure enters the scattering model directly. At a co-polarized residual tolerance of 2 dB, WM produced model-consistent solutions for 425 of 439 retained pixels, compared with 384, 387, and 423 pixels for the exponential, Gaussian, and PE models, respectively. Its blind point ratio was 3.19%, versus 12.53%, 11.85%, and 3.64%, respectively. On the 342 pixels retrievable by all four models, WM gave the lowest mean absolute error for all channels except Sentinel-1 VH. The largest improvement was obtained for Sentinel-1 VV, where WM reduced RMSE to 0.501 dB, compared with 0.820 dB, 0.786 dB, and 0.606 dB for the exponential, Gaussian, and PE models. WM also yielded the most complete retrieval maps and scene mean soil moisture estimates closest to the available SMAP and station reference means. These results show that covariance representation is a material source of structural difference in unregularized multi-sensor SAR inversion.

Check for updates

Academic Editors: Won-Ho Nam, José Darrozes and Dusan Gleich

Received: 11 September 2026
Revised: 21 October 2026
Accepted: 28 October 2026
Published: 30 October 2026

Copyright: © 2026 by the authors. Licensee MDPI, Basel, Switzerland. This article is an open access article distributed under the terms and conditions of the Creative Commons Attribution (CC BY) license.

Keywords: soil moisture; synthetic aperture radar; surface roughness; Whittle–Matérn covariance; physical inversion; bare soil; blind points

1. Introduction

Soil moisture controls land–atmosphere water and energy exchange and affects agricultural water availability, runoff generation, and drought development [1,2]. Synthetic aperture radar (SAR) provides an important means of observing surface soil moisture because microwave backscatter is sensitive to soil dielectric properties and can be acquired under nearly all weather conditions. C-band missions such as Sentinel-1 and RADARSAT-2 further provide multi-polarization and multi-incidence angle observations suitable for high-resolution agricultural monitoring.

Over bare or sparsely vegetated soils, SAR backscatter is governed mainly by soil dielectric properties, surface roughness, radar configuration, and viewing geometry [3–6]. Physically based rough surface scattering models, including the integral equation model (IEM) and its extensions, represent these factors explicitly and have been widely used to simulate co-polarized backscatter from rough bare soils [3–6]. In IEM-type models, surface roughness enters through the height autocorrelation function and the corresponding roughness spectrum [7–11]. The covariance function is therefore not a secondary fitting choice: it controls how roughness spectral energy is distributed over the spatial wavenumbers sampled by the radar.

Exponential and Gaussian covariance functions are commonly adopted because of their simplicity and analytical convenience [3–6]. Both, however, impose fixed covariance and spectral shapes. Agricultural roughness is shaped by tillage, rainfall, surface sealing, aggregation, and row structure, and its effective correlation structure may vary with spatial scale [12]. A fixed covariance form may therefore allocate roughness spectral energy incorrectly over the wavenumber range relevant to SAR scattering.

Field measurements reported by Davidson et al. [12] illustrate this scale dependence. For smooth, non-ploughed surfaces, estimated correlation lengths varied strongly with profile length, whereas ploughed surfaces showed more nearly single-scale behavior. For a smooth harrowed field, an exponential covariance described a short profile reasonably well, but neither the exponential nor the Gaussian covariance represented the same surface over a much longer profile. These results show that a covariance form fitted over limited separations may not represent the effective roughness structure sampled by SAR observations.

This issue has direct consequences for inversion. If the assumed covariance cannot represent the effective roughness spectrum, the resulting forward model mismatch can be compensated by changes in retrieved rms height, correlation length, and soil moisture. An inversion may then produce an acceptable fit for part of the observations while yielding parameters that absorb covariance model error. The central question is therefore not simply which covariance function best fits a measured roughness profile, but whether the covariance structure enlarges the attainable observation domain and reduces compensation among roughness and soil moisture parameters in multi-channel SAR inversion.

The Whittle–Matérn (WM) covariance family provides a structured representation for this problem [13–15]. In addition to a length-scale parameter, it contains a shape parameter, ν, that controls the covariance form and associated roughness spectrum. Under the parameterization used here, the exponential covariance is recovered at $\nu = 0.5$, whereas large ν values approach Gaussian-like behavior. The importance of WM, however, is not merely that it adds an adjustable shape parameter. WM admits a Gaussian–Gamma scale-mixture representation, expressing the covariance as a continuum of Gaussian components

with different effective spatial scales [16]. Thus, ℓ and ν jointly control the distribution of roughness spectral energy across spatial wavenumbers, rather than only the behavior of a single-scale covariance function.

A previous reanalysis of the Davidson et al. measurements showed that WM can represent agricultural surfaces that depart from the canonical exponential and Gaussian forms [16]. For the 25 m profile of a smooth harrowed field, WM increased R^2 from 0.8090 to 0.9726 and reduced RMSE from 0.0871 to 0.0330 relative to the better-performing canonical model. For the 1 m profile, where the exponential model was already adequate, WM still delivered small improvement. These results indicate that the benefit of WM is greatest when the effective roughness structure is not well represented by a fixed exponential or Gaussian covariance.

The powered exponential (PE) covariance provides an important comparison because it also allows the covariance shape to vary through a shape exponent [17,18]. It therefore tests whether shape flexibility alone is sufficient. WM differs from PE in that its Gaussian–Gamma scale-mixture representation links its parameters to a continuum of effective correlation scales and to the resulting roughness spectrum. Comparing WM with PE helps separate the effect of added flexibility from the effect of a multiscale spectral representation.

Our previous work incorporated the WM covariance into the modified extended advanced integral equation model (mEAIEM) and established the required theoretical and numerical framework [11,16]. That study developed the Fourier-domain treatment needed for WM-based backscatter simulation and showed how the smoothness parameter ν controls the multiscale composition of roughness and its scattering response. What remains unresolved is whether this representation improves the reconstruction and inversion of real multi-sensor SAR observations.

Pixel-wise inversion provides a direct test of this question. Unlike spatially regularized retrieval, it does not transfer information among neighboring pixels and therefore exposes whether each observed backscatter vector lies within the attainable domain of a given forward model. Co-registered RADARSAT-2 and Sentinel-1 observations provide multiple co-polarized constraints, making the test more demanding than single channel inversion.

This study evaluates the observational value of the WM covariance for spatially unregularized, pixel-wise SAR inversion over bare agricultural soils. Using co-registered RADARSAT-2 and Sentinel-1 observations, we compare exponential, Gaussian, powered exponential, and WM covariance models within the same mEAIEM framework. All models use the same parameter bounds, objective function, and optimization procedure, isolating the covariance formulation as the main source of structural difference. The analysis focuses on co-polarized backscatter, for which roughness covariance enters the physical scattering formulation directly.

The analysis is limited to C-band because the RADARSAT-2 and Sentinel-1 data provide co-registered, multi-configuration observations at a common wavelength. The WM-mEAIEM framework can be applied to L-band or combined L-/C-band observations. However, sensitivity to surface roughness and soil conditions varies with wavelength. Consequently, the effects of covariance model misspecification and the relative performance of the covariance models may differ at L-band. Assessing this frequency dependence is beyond the scope of the present study.

We define a "blind point" as a pixel for which the observed multi-channel co-polarized backscatter vector cannot be reconstructed within the prescribed parameter bounds and residual tolerance. The blind point ratio therefore measures the fraction of observations outside the practically attainable domain of a given covariance model under a common inversion configuration. Reconstruction errors are evaluated both over the pixels retrieved by each model and over the common subset retrieved by all models.

The study addresses three questions:

1. Does the WM covariance reduce blind point occurrence and improve multi-sensor co-polarized backscatter reconstruction relative to the exponential and Gaussian covariance models?
2. Does WM provide advantages over PE, indicating that a multiscale scale-mixture representation offers more than additional covariance-shape flexibility?
3. Does WM yield scene mean soil moisture estimates that are more consistent with the available SMAP and in situ reference means, while reducing model-dependent discrepancies in the retrieved soil moisture?

The remainder of this paper is organized as follows. Section 2 describes the study area, SAR datasets, and preprocessing strategy, and presents the WM roughness representation, scattering models, pixel-wise inversion strategy, and blind point metric. Section 3 presents the numerical experimental results. Section 4 discusses their physical interpretation, limitations, and implications for future soil moisture retrieval studies. Finally, Section 5 summarizes the main findings and concludes the paper.

2. Materials and Methods

2.1. Study Area, SAR Data, and Field Measurements

This study is conducted in Lishu County, Jilin Province, China (43.203222°–43.206000°N, 124.233417°–124.234889°E). The soil comprises 21.82% sand, 4.18% clay, and approximately 74.00% silt. The site is primarily agricultural cropland and was under bare soil conditions during the SAR acquisitions.

RADARSAT-2 and Sentinel-1 data were acquired on 13 April 2026, at 09:26 UTC and 11 April 2026, at 21:54 UTC, respectively, with a temporal separation of approximately 35.5 h. Precipitation data from the China Meteorological Administration Land Data Assimilation System (CLDAS) indicated no rainfall during this period. Field level irrigation and tillage records were unavailable; therefore, changes in soil moisture or surface conditions between acquisitions cannot be excluded. The observations are consequently treated as quasi-coincident rather than strictly simultaneous.

RADARSAT-2 data were acquired in Fine Quad-Pol mode at 5.4 GHz, with local incidence angles of 24.5°–26.4°. Sentinel-1 data were acquired in Interferometric Wide (IW) mode at 5.4 GHz, with local incidence angles of 31.2°–32.4°. Both datasets were terrain-corrected using the same DEM and co-registered to a common grid with a spatial grid spacing (pixel size) of 7.52 m × 10.28 m, resulting in exactly 480 pixels within the study area.

Figure 1 illustrates the geographic setting of the study area and its topographic, vegetation, and land cover characteristics. Figure 1a and 1b locate the study area at national and regional scales, respectively, whereas Figure 1c shows the local agricultural landscape in Google Earth imagery acquired on 13 June and 17 August 2025. The study area is located in a typical agricultural region near Lishu County, Northeast China, and is dominated by cropland intersected by farm roads.

Figure 1d–f present auxiliary datasets: the SRTM 1 Arc-Second Global DEM [19], NDVI derived from Sentinel-2 imagery acquired at 02:45:48 UTC on 7 April 2026, and the GlobeLand30 land cover dataset produced by the National Geomatics Center of China [20]. All auxiliary datasets were resampled onto a common SAR-aligned grid, using bilinear interpolation for DEM and NDVI and area-weighted majority voting for GlobeLand30. Elevation ranges from approximately 158 to 168 m, indicating generally flat terrain with limited topographic variation. NDVI values are predominantly below 0.2, consistent with sparse vegetation and the bare soil conditions required for the subsequent inversion. GlobeLand30

identifies an impervious-surface strip in the northern part of the study area. Its location and geometry closely match the farm roads visible in the high-resolution Google Earth imagery; these pixels were therefore excluded when constructing the final bare soil mask.

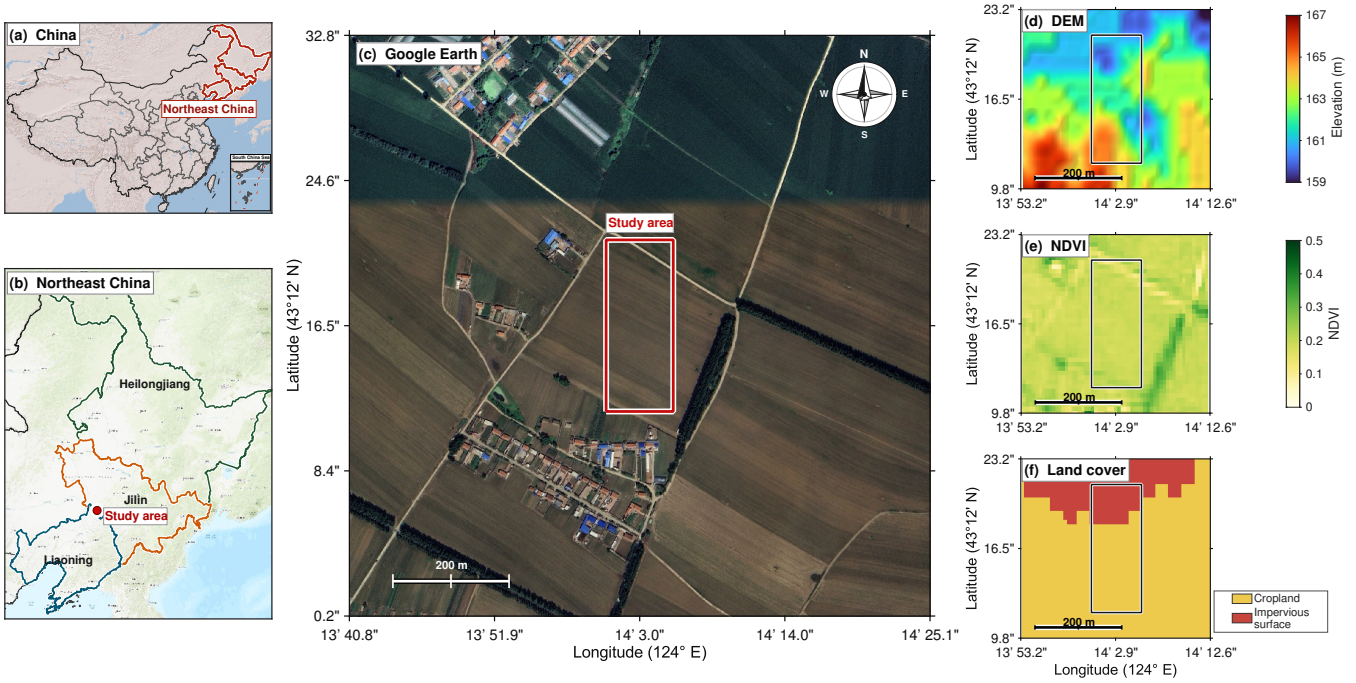


Figure 1. Study area and auxiliary geographic datasets: (**a**) location of Northeast China within China, (**b**) location of the study area in Northeast China, (**c**) Google Earth imagery acquired on 13 June 2025 and 17 August 2025, (**d**) SRTM DEM, (**e**) NDVI derived from Sentinel-2 imagery acquired on 7 April 2026, and (**f**) GlobeLand30 land cover classification. The red marker in (**b**) indicates the location of the study area, while the red rectangle in (**c**) and the black rectangles in (**d**–**f**) indicate the study area boundary.

The five soil moisture stations used in this study are Lishu (54154; 124.3142°E, 43.3064°N), Lishu Liujiagangzi (E4055; 124.5608°E, 43.4994°N), Lishu Miaopu (E0131; 124.2903°E, 43.2922°N), Lishu Quanyangou (E0134; 124.4381°E, 43.2725°N), and Changtu (L7532; 123.9531°E, 42.8928°N). Each station records daily volumetric soil moisture at a depth of 10 cm. For each station, the reference value was calculated as the mean of daily observations from 8 to 13 April 2026.

The locations of the SMAP Level-4 grid and the five soil moisture stations are shown in Figure 2. The station observations are used as supplementary regional references rather than for pixel-scale validation. Their measurement depth of 10 cm differs from the shallow surface layer primarily sensed by C-band SAR, and none of the stations is located within the study area. The two nearest stations are approximately 12 km from the study area. Although the site lies on the relatively flat Northeast China Plain, soil moisture variability over this distance may limit the representativeness of the station measurements.

SMAP Level-4 soil moisture is therefore used as the primary scene scale reference because its grid covers the study area. The station measurements provide complementary information on regional soil moisture conditions. They are used to assess whether the scene mean soil moisture retrieved from SAR is consistent with the overall moisture level and wetness conditions during the SAR acquisition period.

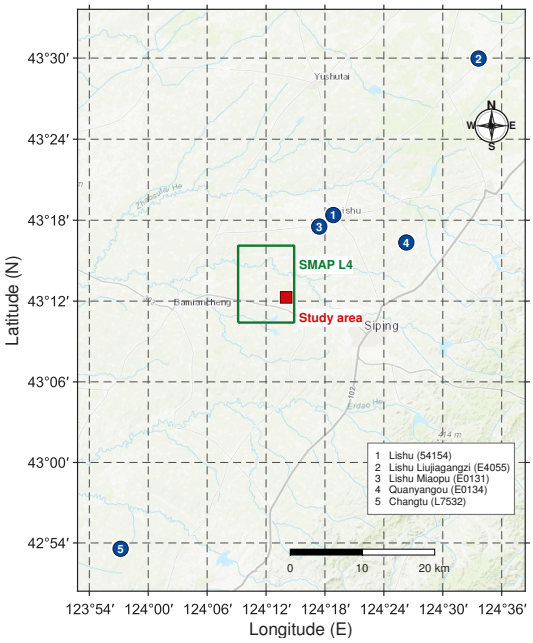


Figure 2. Locations of the five soil moisture stations and the SMAP Level-4 grid. The red square marks the study area, the green rectangle outlines the SMAP Level-4 grid, and the blue circles indicate the soil moisture stations.

2.2. Multi-Sensor Backscatter Dataset

The retrieval experiment uses the overlapping bare soil pixels covered by both the RADARSAT-2 and Sentinel-1 acquisitions. The RADARSAT-2 observation vector includes HH, VV, and HV backscatter coefficients, while the Sentinel-1 vector contains VV and VH backscatter coefficients. Following radiometric calibration, co-registration, incidence angle processing, quality control, and bare soil masking, the multi-sensor observation vector for each pixel is defined as

$$\boldsymbol{\sigma}^{0,\mathrm{obs}} = \left[\sigma_{HH}^{0,\mathrm{RS2}},\ \sigma_{VV}^{0,\mathrm{RS2}},\ \sigma_{HV}^{0,\mathrm{RS2}},\ \sigma_{VV}^{0,\mathrm{S1}},\ \sigma_{VH}^{0,\mathrm{S1}}\right]^{T}. \tag{1}$$

Only pixels available in both datasets are retained. Vegetated areas, urban areas, water bodies, farm roads, layover and shadow regions, and pixels with missing observations are excluded. Out of the 480 total grid cells within the study bounding box, 41 cells are identified as farm roads or non-soil features. This leaves exactly 439 bare soil pixels as the final dataset used for the inversion models. These pixels provide broad spatial coverage and support stable statistical evaluation of the inversion results. Nevertheless, neighboring pixels may be spatially correlated; therefore, this pixel count should not be regarded as the number of fully independent samples. The reported statistics are consequently interpreted as evaluations over spatially distributed retrievals. The consistent performance patterns observed across polarization channels and roughness covariance models indicate that the main conclusions are not driven by a small number of individual pixels.

2.3. Preprocessing Strategy

Radiometric calibration, geometric co-registration, incidence angle processing, quality control, and bare soil masking are applied before the multi-sensor analysis. Both datasets were terrain-corrected and projected to the common analysis grid using the same DEM. The local incidence angle was retained at the pixel level and used directly as an input to the forward scattering model. For Sentinel-1, the local incidence angle was derived in SNAP during Range-Doppler terrain correction using the DEM-based local incidence angle geometry. For RADARSAT-2, the HV and VH channels were averaged in linear power units under

the reciprocity assumption to form a single cross-polarized observation. This averaging reduces random variation in an individual cross-polarized measurement. For Sentinel-1, `COPERNICUS/S1_GRD` collection in Google Earth Engine was used. The product had already undergone thermal noise removal, radiometric calibration, and terrain correction using the Sentinel-1 Toolbox, with the terrain-corrected backscatter converted to decibel units. These steps are particularly relevant to the lower-intensity VH channel, for which noise related effects may be more pronounced. No speckle filtering is applied to either the RADARSAT-2 or Sentinel-1 backscatter data.

This choice is made to preserve the native pixel scale radiometric observations used in the inversion. Spatial speckle filters reduce local radiometric variability by combining information from neighboring pixels and can introduce filter-dependent spatial dependence among the resulting backscatter values. Such processing may modify local backscatter contrasts and the distribution of model observation residuals. It could therefore confound the present comparison, which is designed to isolate the effect of the assumed roughness covariance representation within a common pixel-wise inversion framework.

Thus, although residual speckle remains a component of observational uncertainty in the pixel-wise reconstruction experiment, all covariance formulations are evaluated using the same unfiltered and co-registered observations, parameter bounds, residual criterion, and optimization procedure. Differences in blind point ratio and reconstruction performance can therefore be attributed to the relative ability of the respective covariance formulations to represent the observed multi-sensor backscatter vectors within the common inversion framework.

2.4. Study Design and Hypotheses

This study examines whether a flexible Whittle–Matérn roughness covariance representation reduces structural mismatch in pixel-wise, multi-sensor SAR backscatter inversion over bare agricultural soil. The analysis compares four roughness correlation assumptions: exponential, Gaussian, PE, and WM.

The primary hypothesis is that the WM representation provides a broader physically attainable co-polarized backscatter domain than fixed form correlation functions. Accordingly, the WM model is expected to yield: (i) a lower fraction of model inconsistent pixels, and (ii) lower optimized backscatter residuals under the same parameter bounds and observation configuration.

The analysis evaluates within sample model consistency rather than independent soil moisture retrieval accuracy. Because the same SAR observations are used for parameter estimation and reconstruction assessment, improved agreement between modeled and observed backscatter is interpreted as reduced forward model mismatch, not as direct proof of improved predictive soil moisture accuracy.

2.5. SAR Observation Vector and Preprocessing

For each retained bare soil pixel, the multi-sensor SAR observation vector is defined in the dB unit as

$$\mathbf{y}^{\mathrm{obs}} = \left[\sigma^{0,\mathrm{RS2}}_{HH,\mathrm{dB}}, \sigma^{0,\mathrm{RS2}}_{VV,\mathrm{dB}}, \sigma^{0,\mathrm{RS2}}_{HV,\mathrm{dB}}, \sigma^{0,\mathrm{S1}}_{VV,\mathrm{dB}}, \sigma^{0,\mathrm{S1}}_{VH,\mathrm{dB}}\right]^{T}. \quad (2)$$

All SAR data are radiometrically calibrated, terrain corrected, co-registered to a common analysis grid, and converted to local incidence angle geometry. The preprocessing workflow should ensure that the same ground location is represented by each element of Equation (2). Pixels affected by water, urban land cover, radar shadow, layover, missing data, or non-bare soil conditions are excluded.

Bare soil selection is based on a Sentinel-2 normalized difference vegetation index (NDVI) threshold of less than 0.2, the GlobeLand30 land cover product, and visual interpretation of high resolution Google Earth imagery.

2.6. Roughness Covariance Models

The surface height field is assumed to be second-order stationary and isotropic within an individual SAR pixel. Let s denote the rms surface height and let r denote horizontal lag distance. The normalized WM correlation function is written as

$$\rho_{\mathrm{WM}}(r;\ell,\nu) = \frac{2^{1-\nu}}{\Gamma(\nu)}\left(\sqrt{2\nu}\frac{r}{\ell}\right)^{\nu} K_{\nu}\left(\sqrt{2\nu}\frac{r}{\ell}\right), \tag{3}$$

where $\ell > 0$ is the WM length scale, $\nu > 0$ is the smoothness parameter, $\Gamma(\cdot)$ is the gamma function, and $K_{\nu}(\cdot)$ is the modified Bessel function of the second kind. The corresponding covariance function is

$$C_{\mathrm{WM}}(r) = s^2 \rho_{\mathrm{WM}}(r;\ell,\nu). \tag{4}$$

The exponential correlation function is obtained as the special WM case $\nu = 0.5$:

$$\rho_{\mathrm{Exp}}(r;\ell) = \exp\left(-\frac{r}{\ell}\right). \tag{5}$$

where ℓ coincidences with the correlation length.

The Gaussian correlation function is considered as a separate canonical roughness model:

$$\rho_{\mathrm{Gau}}(r;\ell_g) = \exp\left[-\left(\frac{r}{\ell_g}\right)^2\right], \tag{6}$$

where ℓ_g is the Gaussian correlation length.

The powered exponential correlation function is expressed as

$$\rho_{\mathrm{PE}}(r;\ell) = \exp\left[-\left(\frac{r}{\ell}\right)^{\alpha}\right]. \tag{7}$$

In this study, the correlation length ℓ_c follows the strict convention that it is defined as the separation distance at which the correlation function decreases to $1/e$ of its value at zero lag. This quantity is, in general, distinct from the WM length-scale parameter ℓ. Although ℓ_c cannot be expressed analytically as a function of ℓ, the WM correlation function $C_{\mathrm{WM}}(r)$ decreases monotonically with separation distance r for a given smoothness parameter ν. This monotonicity enables an efficient numerical mapping between the physically interpretable correlation length ℓ_c and the WM length-scale parameter ℓ.

2.7. WM Spectral Terms for mEAIEM

The roughness covariance function enters the mEAIEM formulation through the spectral terms associated with powers of the normalized correlation function. To avoid ambiguity in roughness amplitude scaling, the n-th order roughness spectrum is defined here as

$$\mathcal{W}_R^{(n)}(k) = 2\pi \int_0^{\infty} [\rho_R(r)]^n J_0(kr)\, r\, dr, \tag{8}$$

where $R \in \{\mathrm{Exp}, \mathrm{Gau}, \mathrm{PE}, \mathrm{WM}\}$, $J_0(\cdot)$ is the zeroth order Bessel function of the first kind, and k is the radial spatial wavenumber. Under this convention, rms height is represented explicitly by the factor s^{2n} in the mEAIEM scattering expansion.

For $n = 1$, the normalized WM spectrum has the analytic form

$$\mathcal{W}_{\mathrm{WM}}^{(1)}(k) = \frac{2\pi\ell^2}{\left(1 + \dfrac{k^2\ell^2}{2\nu}\right)^{\nu+1}}. \tag{9}$$

For higher-order terms, direct numerical Hankel integration of Equation (8) can become oscillatory. We therefore use the Gaussian–Gamma mixture representation [16]

$$\rho_{\mathrm{WM}}(r) = \int_0^\infty \exp\left(-\frac{r^2}{4u}\right) f_{\nu,\ell}(u)\, du, \tag{10}$$

where

$$f_{\nu,\ell}(u) = \frac{1}{\Gamma(\nu)} \left(\frac{2\nu}{\ell^2}\right)^{\nu} u^{\nu-1} \exp\left(-\frac{2\nu u}{\ell^2}\right). \tag{11}$$

This representation allows to express $\rho_{\mathrm{WM}}(r)$ as a scale mixture of Gaussian kernels $\exp(-r^2/(4u))$ with a Gamma-distributed scale parameter u. The Whittle–Matérn process is thus interpretted probabilistically as a superposition of rescaled Gaussian processes.

This representation gives a stable, non-oscillatory form for the n-th order WM spectrum [16]:

$$\mathcal{U}^{(n)}_{\mathrm{WM}}(k) = \int \cdots \int \frac{4\pi}{t} \exp\left(-\frac{k^2}{t}\right) \prod_{i=1}^{n} f_{\nu,\ell}(u_i)\, du_i, \qquad t = \sum_{i=1}^{n} \frac{1}{u_i}. \tag{12}$$

Unlike the conventional Hankel-transform representation, Equation (12) contains no oscillatory integrand and is therefore well suited to stable numerical evaluation. Moreover, the integrand remains well behaved as $t \to 0$, since $t^{-1} \exp(-k^2/t) \to 0$ for $k > 0$. Because $f_{\nu,\ell}(u_i)$ is a probability density, the multiple integral can also be interpreted as an expectation $\mathbb{E}[\frac{4\pi}{t} \exp\left(-\frac{k^2}{t}\right)]$ over independent random variables $u_i \sim f_{\nu,\ell}$. This interpretation enables Monte Carlo evaluation without introducing recursive or combinatorial dependence as the scattering order n increases; each additional integration dimension requires only one additional independent random draw. In the present implementation, Equation (12) is evaluated using a hybrid strategy combining numerical quadrature and Monte Carlo sampling. The implementation is verified by recovering the analytic first-order spectrum and the exponential limit at $\nu = 0.5$.

2.8. Forward Backscatter Model

For each roughness representation $R \in \{\mathrm{Exp}, \mathrm{Gau}, \mathrm{PE}, \mathrm{WM}\}$, co-polarized backscatter is simulated using the corresponding mEAIEM implementation:

$$\sigma^{0,\mathrm{mod}}_{p,R} = \mathcal{F}^{\mathrm{mEAIEM}}_{p,R}(s, \ell_R, \nu_R, m_v, \theta_i, \boldsymbol{\eta}), \tag{13}$$

where p denotes polarization, m_v is volumetric soil moisture, θ_i is local incidence angle, and $\boldsymbol{\eta}$ denotes fixed ancillary inputs, including soil texture, soil temperature, and the dielectric mixing model parameters. The argument ν_R is the smoothness parameter ν for WM model, and the exponent parameter α for PE model. For the exponential and Gaussian cases, the parameter ν_R is not estimated.

The cross-polarized channels are simulated using an empirical Oh-type model [21]:

$$\sigma^{0,\mathrm{mod}}_{xp} = \mathcal{F}^{\mathrm{Oh}}(s, \ell_R, m_v, \theta_i, \boldsymbol{\eta}). \tag{14}$$

The modeled five channel observation vector in dB is

$$\mathbf{f}_R(\boldsymbol{\theta}_R) = \begin{bmatrix} \sigma^{0,\mathrm{mod}}_{HH,\mathrm{RS2},R} \\ \sigma^{0,\mathrm{mod}}_{VV,\mathrm{RS2},R} \\ \sigma^{0,\mathrm{mod}}_{HV,\mathrm{RS2},R} \\ \sigma^{0,\mathrm{mod}}_{VV,\mathrm{S1},R} \\ \sigma^{0,\mathrm{mod}}_{VH,\mathrm{S1},R} \end{bmatrix}. \tag{15}$$

2.9. Pixel-Wise Multi-Sensor Inversion

The WM parameter vector is

$$\boldsymbol{\theta}_{\mathrm{WM}} = [s,\ \ell,\ \nu,\ m_v]^T, \tag{16}$$

whereas the exponential, Gaussian, and PE parameter vectors are

$$\boldsymbol{\theta}_{\mathrm{Exp}} = \left[s,\ \ell_{\mathrm{Exp}},\ m_v\right]^T, \qquad \boldsymbol{\theta}_{\mathrm{Gau}} = [s,\ \ell_{\mathrm{Gau}},\ m_v]^T, \qquad \boldsymbol{\theta}_{\mathrm{PE}} = [s,\ \ell_{\mathrm{PE}},\ \alpha,\ m_v]^T. \tag{17}$$

For each pixel and each roughness representation, the inversion minimizes the weighted relative difference between observed and modeled backscatter in dB power units to limit the disproportionate influence of cross-polarized channels in the joint inversion:

$$J_R(\boldsymbol{\theta}_R) = \sum_{k=1}^{5} w_k \left[\frac{\sigma_k^{0,\mathrm{obs}} - \sigma_{k,R}^{0,\mathrm{mod}}(\boldsymbol{\theta}_R)}{\sigma_k^{0,\mathrm{obs}}} \right]^2. \tag{18}$$

The pixel-wise estimate is

$$\hat{\boldsymbol{\theta}}_R = \underset{\boldsymbol{\theta}_R \in \Omega_R}{\arg\min}\, J_R(\boldsymbol{\theta}_R), \tag{19}$$

where Ω_R denotes the physically plausible parameter domain for model R. The adopted bounds, channel weights, and optimizer settings are specified in the numerical experiment.

The same five channel observations, parameter bounds, initialization strategy, and optimization settings are used for all four roughness representations. Thus, differences in inversion performance can be attributed to the assumed roughness correlation structure rather than to differences in the observation configuration.

For each pixel and roughness model R, the minimum weighted residual distance is defined as

$$d_{\min,R} = \left[\sum_{k=1}^{5} w_k \left(\sigma_k^{0,\mathrm{obs}} - \sigma_{k,R}^{0,\mathrm{mod}}\left(\hat{\boldsymbol{\theta}}_R\right) \right)^2 \right]^{1/2}, \tag{20}$$

where $\hat{\boldsymbol{\theta}}_R$ is obtained from Equation (19).

Thus, $d_{\min,R}$ is not strictly the shortest weighted distance between the observed five-channel backscatter vector and the set of all backscatter vectors attainable by model R within the prescribed parameter domain. Rather, it is the weighted residual distance evaluated at the parameter vector that minimizes the weighted relative difference between the observed and modeled backscatter.

This metric also differs from the blind point screening criterion. Blind point screening is based on the maximum absolute residual in the co-polarized channels; the cross-polarized channel is excluded, and the co-polarized channels are evaluated separately. In contrast, $d_{\min,R}$ represents the combined residual across all five channels, including both co-polarized and cross-polarized observations, with each channel weighted by w_k.

2.10. Model Consistency and Feasible Domain Metric

The primary comparison among roughness representations is based on the ability to reproduce the co-polarized observations, for which the roughness covariance enters the mEAIEM formulation directly. The co-polarized channel set is

$$\mathcal{K}_{\mathrm{copol}} = \{\mathrm{RS2}\text{-}HH,\ \mathrm{RS2}\text{-}VV,\ \mathrm{S1}\text{-}VV\}. \tag{21}$$

For pixel j, channel k, and roughness representation R, the optimized dB residual is

$$e_{j,k,R}^{\mathrm{dB}} = f_{j,k,R}\left(\hat{\boldsymbol{\theta}}_{j,R}\right) - y_{j,k}^{\mathrm{obs}}. \tag{22}$$

The maximum absolute co-polarized residual is defined as

$$q_{j,R} = \max_{k \in \mathcal{K}_{\text{copol}}} \left| e^{\text{dB}}_{j,k,R} \right|. \tag{23}$$

A pixel is classified as model-consistent under roughness representation R when

$$q_{j,R} \leq \epsilon, \tag{24}$$

where ϵ denotes the prescribed residual tolerance for co-polarized backscatter reconstruction. In this study, a tolerance of $\epsilon = 2$ dB is adopted, consistent with error magnitudes commonly reported for bare soil SAR backscatter modeling, for which model observation discrepancies of approximately 2 dB are generally regarded as acceptable simulation performance [22,23]. Pixels that do not satisfy this criterion are classified as model inconsistent. Hereafter, such pixels are referred to as blind points, because their observed co-polarized backscatter vectors fall outside the practically attainable backscatter domain of representation R, given the prescribed parameter bounds and common inversion framework.

The model inconsistency fraction, equivalently the blind point ratio, is defined as

$$\text{MIFR}_R = \frac{1}{N} \sum_{j=1}^{N} \mathbb{I}\left(q_{j,R} > \epsilon\right), \tag{25}$$

where N is the number of retained bare soil pixels and $\mathbb{I}(\cdot)$ is the indicator function.

2.11. Statistical Comparison and Evaluation Sets

Backscatter reconstruction metrics, including RMSE, MAE, bias, and Pearson correlation coefficient, are calculated in the dB domain. Metrics are reported for both:

1. Model-specific model-consistent pixels;
2. The common model-consistent subset,

$$\mathcal{S}_{\text{common}} = \mathcal{S}_{\text{Exp}} \cap \mathcal{S}_{\text{Gau}} \cap \mathcal{S}_{\text{PE}} \cap \mathcal{S}_{\text{WM}}. \tag{26}$$

Because neighboring SAR pixels are spatially correlated, uncertainty in the model-performance statistics was estimated using a spatial block bootstrap rather than assuming pixel-wise independence. Block size was selected according to the spatial autocorrelation range and field geometry of the study area. A 2 × 2-pixel block was used to preserve the dominant local spatial dependence while retaining sufficient resampling units.

Overlapping 2 × 2-pixel blocks were constructed across the study area and treated as resampling units. For each bootstrap replicate, blocks were sampled with replacement, and the blind point ratio and reconstruction-error metrics were recalculated. The procedure was repeated 1000 times. Bootstrap 95% confidence intervals were derived from the 2.5th and 97.5th percentiles and are reported with the model-comparison results. These intervals quantify the sensitivity of the results to spatial sample composition while accounting for local spatial dependence.

3. Results

This section compares pixel-wise inversion results obtained using the exponential, Gaussian, powered exponential (PE), and Whittle–Matérn (WM) roughness representations. The inversions use quasi-coincident RADARSAT-2 and Sentinel-1 observations over the overlapping bare soil area. All parameters are retrieved independently for each pixel, without sliding window processing or local roughness constancy constraints.

The analysis addresses three questions: (1) how often each roughness representation reproduces the co-polarized SAR observations within the specified tolerance; (2) how accurately the optimized parameters reconstruct the five-channel SAR observations; and (3) how the retrieved roughness, WM smoothness, and soil moisture parameters vary across the study area.

3.1. Pixel-Wise Multi-Sensor Inversion Configuration

Pixel-wise inversions are performed independently for all retained bare soil pixels using the four roughness covariance models described in Section 2.6. The parameter vectors, forward scattering models, parameter bounds, and bounded optimization framework are defined in Sections 2.8 and 2.9.

All experiments use the same co-registered five channel RADARSAT-2 and Sentinel-1 dataset, ancillary inputs, initialization procedure, multi-start configuration, stopping criteria, and optimizer settings. Thus, the roughness covariance representation is the only difference among the inversion experiments.

The RADARSAT-2 co-polarized HH and VV channels and the Sentinel-1 VV channel are simulated using the mEAIEM formulation. The RADARSAT-2 HV and Sentinel-1 VH channels are simulated using the same Oh-type semi-empirical model in all experiments. The five channels are jointly inverted to constrain roughness and soil moisture parameters. The Dobson dielectric mixing model [24] is employed to relate the soil moisture to the soil dielectric constant for the site-specific soil texture.

Equal weights are assigned to all channels in the reference configuration. This avoids imposing an a priori preference for a particular sensor or polarization. The relative residual formulation naturally normalizes the contributions of channels with differing backscatter magnitudes. Sensitivity tests with alternative weighting schemes produced consistent model rankings and did not affect the main conclusion that the WM representation provides the best reconstruction performance. Therefore, only the equal weight results are presented.

No spatial regularization, moving window averaging, or neighborhood-based roughness constraint is applied. Each pixel is inverted solely from its own multi-sensor SAR observations, providing a direct test of the ability of each roughness covariance representation to reproduce local backscatter behavior without information transfer from neighboring pixels.

Table 1 lists the parameter bounds used in the pixel-wise inversions. Volumetric soil moisture (m_v) is bounded between 0.001 and 0.7 $cm^3\ cm^{-3}$. The lower bound accommodates near dry conditions while avoiding numerical singularities at zero, whereas the upper bound permits solutions under high moisture conditions [25–27]. The *rms* height (s) and correlation length (ℓ) are bounded within $[0.001, 0.05]$ m and $[0.001, 0.5]$ m, respectively [28]. For the PE model, the exponent parameter α is bounded between 1 and 2 [29,30]. For the WM model, the smoothness parameter ν is bounded within $[0.001, 10]$. These broad ranges encompass a wide range of agricultural soil moisture and roughness conditions and allow potential parameter compensation and boundary clustering effects to be identified.

Before optimization, all parameters are scaled to $[0, 1]$ using their respective bounds, and the physical constraint $s \leq \ell$ is imposed. To reduce sensitivity to local minima, we use a hybrid coarse-grid and local optimization strategy. The objective function is first evaluated on a predefined parameter grid, and the four parameter combinations with the lowest objective values are used to initialize constrained local optimization with an interior-point algorithm. The solution with the lowest objective value among the four local runs is retained for each pixel. For s, ℓ, m_v, and α, the coarse grid includes the 10%, 50%, and 90% positions of the respective search intervals. For the WM smoothness parameter ν, grid points are logarithmically spaced following the sensitivity analysis of [16]. The maximum number of function evaluations is 1000, and the step tolerance is 10^{-8}. All models use the same parameter bounds, initialization strategy, and local optimization settings to ensure a consistent comparison.

Table 1. Parameter bounds used in the pixel-wise inversion.

Parameter	Unit	Lower Bound	Upper Bound
Volumetric soil moisture m_v	$cm^3\ cm^{-3}$	0.001	0.7
RMS height s	m	0.001	0.05
Correlation length ℓ	m	0.001	0.5
PE shape parameter α	–	1	2
WM smoothness parameter ν	–	0.001	10

3.2. Model Consistency and Blind Point Analysis

Although the bounded optimization procedure yields a numerical solution for each retained bare soil pixel, the resulting parameter set does not necessarily reproduce the observed multi-sensor backscatter within the prescribed tolerance. Model consistency is therefore assessed using the co-polarized residual criterion defined in Section 2.10.

The assessment uses the RADARSAT-2 HH and VV channels and the Sentinel-1 VV channel. These channels are selected because the main difference among the four inversion experiments is the roughness covariance representation in the mEAIEM co-polarized scattering model. In contrast, the RADARSAT-2 HV and Sentinel-1 VH are simulated using the same Oh-type empirical model for all roughness representations. Their residuals therefore do not distinguish the attainable co-polarized backscatter domains of the exponential, Gaussian, PE, and WM covariance models. In addition, cross-polarized backscatter is more susceptible to limitations of the empirical model, noise floor effects, residual vegetation contributions, and sensor-dependent differences.

Table 2 summarizes the model-consistency results. The exponential and Gaussian models identify 55 and 52 blind pixels, corresponding to 12.53% and 11.85%, respectively, of the 439 retained bare soil pixels. The PE model reduces the number of blind pixels to 16, corresponding to a blind point ratio of 3.64%. The WM model achieves the highest consistency, with 14 blind pixels, or 3.19% of the study area.

Table 2. Model-consistency results for pixel-wise multi-sensor inversion under different roughness assumptions.

Roughness Assumption	Bare Soil Pixels	Model-Consistent Pixels	Blind Points	Blind Point Ratio (%)	95% CI (%)
Exponential	439	384	55	12.53	[7.00, 15.78]
Gaussian	439	387	52	11.85	[8.45, 15.95]
Powered Exponential	439	423	16	3.64	[1.79, 6.34]
Whittle–Matérn	439	425	14	3.19	[1.35, 5.64]

Relative to the exponential and Gaussian models, the WM model reduces the blind point ratio by approximately 74.5% and 73.1%, respectively. Under identical parameter bounds, residual thresholds, and optimization settings, both the PE and WM models expand the attainable backscatter domain, with the WM model providing the greatest coverage. In the spatial block bootstrap analysis, the 95% confidence interval of the WM blind point ratio is the lowest and does not overlap with those of the exponential and Gaussian models. This result indicates that the improved WM performance remains robust after accounting for spatial autocorrelation and is not caused by localized spatial anomalies.

Figure 3 shows the sensitivity of the blind point ratio to the residual threshold. As the threshold increases from 1.5 dB to 5.0 dB, the blind point ratio decreases monotonically for

all models because a less stringent tolerance allows more pixels to satisfy the consistency criterion. The largest separation among models occurs between 1.5 and 2.0 dB, where WM and PE yield substantially lower ratios than the fixed exponential and Gaussian covariance models. Above 4.0 dB, the ratios for all models approach zero and the differences diminish. Nevertheless, WM retains the lowest blind point ratio across the full threshold range, indicating that its superior consistency is not an artifact of the selected 2.0 dB threshold.

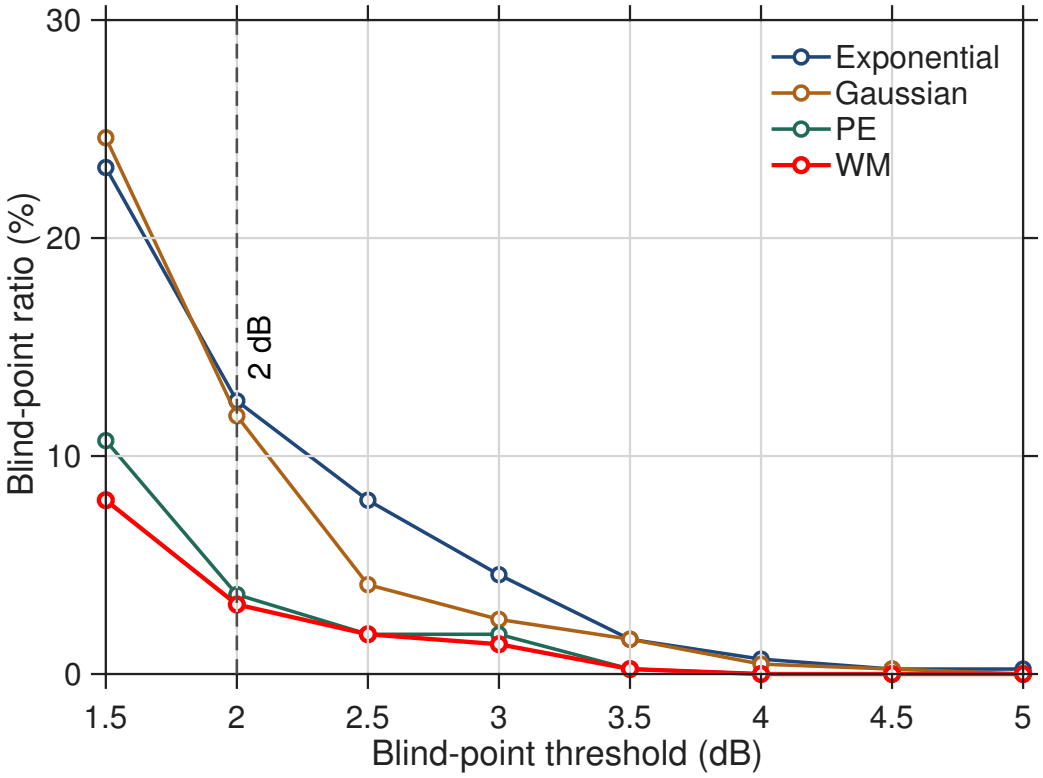


Figure 3. Sensitivity of the blind point ratio to the decision threshold for the different roughness models.

3.3. Residual Analysis

Figure 4 compares the distributions of $d_{\min,R}$ for the four roughness models. The distributions overlap partially, indicating that all models can satisfactorily reconstruct the observations for some pixels. However, their overall shapes differ systematically.

The WM distribution is concentrated at lower residual values and shows substantial density near $d_{\min} = 0$. Its primary mode occurs at a lower residual level than those of the other models. The exponential model has a relatively sharp mode at low-to-moderate residual values but a broader high-residual tail. The PE distribution resembles that of the exponential model, with a slightly higher peak and greater density near $d_{\min} = 0$. The Gaussian distribution is shifted toward larger residual distances, with its primary mode near $d_{\min} = 2$. All models show a small secondary group at high residual values, around $d_{\min} \approx 8$–9.

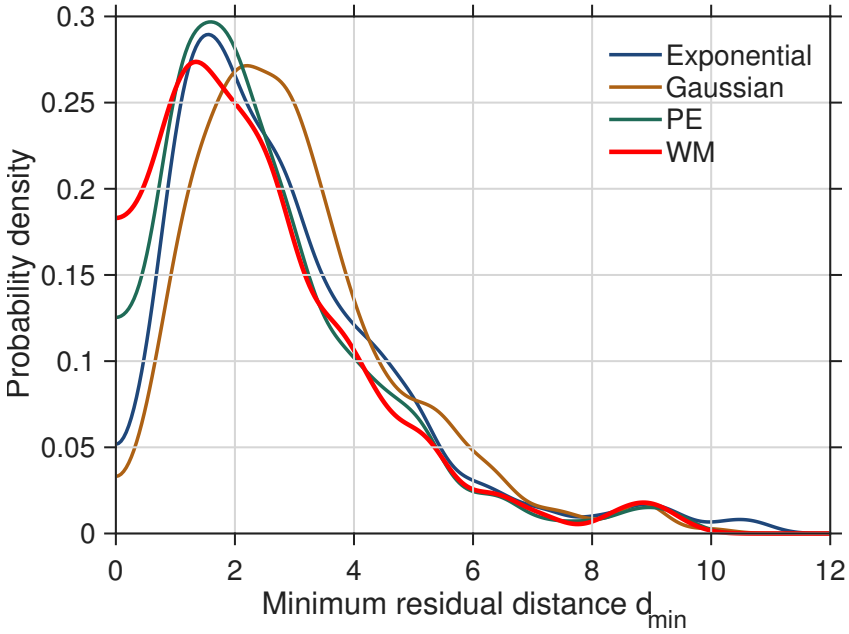


Figure 4. Distribution of minimum residual distances (dB) for the exponential, Gaussian, PE, and WM roughness models.

3.4. Spatial Distribution of Blind Pixels

Figure 5 illustrates the spatial distribution of model-consistent (black) and blind (white) pixels obtained under the exponential, Gaussian, powered exponential (PE), and Whittle–Matérn (WM) roughness covariance models. Gray pixels represent areas excluded from the inversion, such as roads and non-bare soil surfaces.

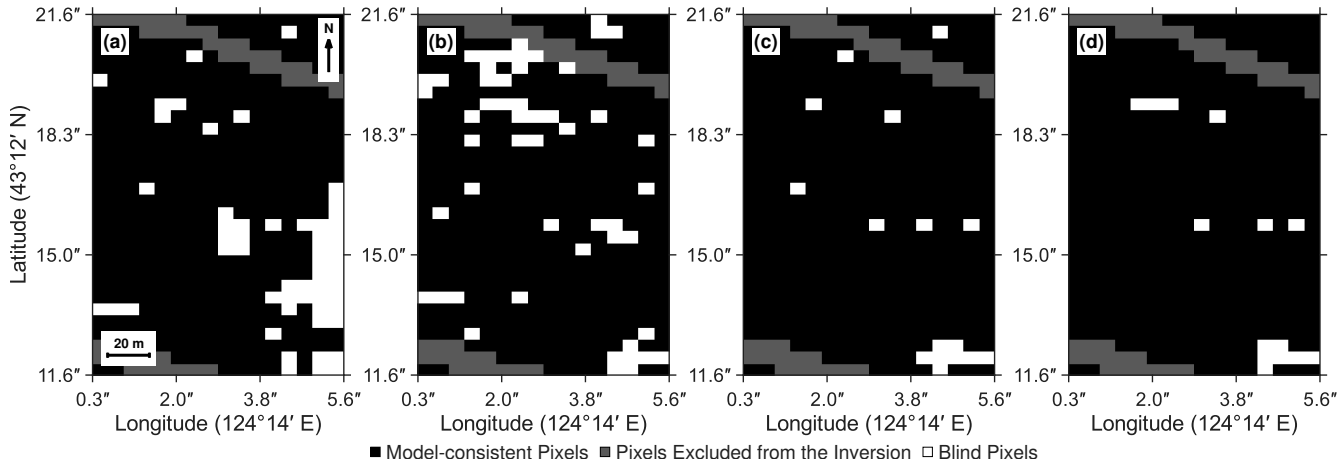


Figure 5. Spatial distribution of model-consistent pixels (black), pixels excluded from the inversion (gray), and blind pixels (white) under four roughness covariance models: (**a**) exponential, (**b**) Gaussian, (**c**) PE, and (**d**) WM.

The exponential and Gaussian models produce similar numbers of blind pixels. These pixels occur partly in spatial clusters rather than appearing only as isolated points, indicating that the mismatches are associated with local surface conditions rather than numerical effects alone.

In contrast, both the PE and WM models substantially reduce the blind pixel count. Under the PE assumption, the remaining blind pixels are scattered across the northeastern, central, and southeastern regions, reflecting a broader coverage of model-consistent solutions. The WM model further reduces the blind pixel count, leaving only a sparse set of blind pixels concentrated primarily in the central portion of the study area.

3.5. Multi-Channel Backscatter Reconstruction Performance

The optimized parameter sets are inserted into their corresponding forward models to reconstruct the five SAR backscatter channels, which are then compared with the satellite observations. Because the observations are also used in the inversion, these results evaluate reconstruction consistency rather than independent predictive performance.

All metrics are calculated in dB. For each channel, the RMSE, MAE, and bias are defined as

$$\mathrm{RMSE} = \sqrt{\frac{1}{N}\sum_{j=1}^{N}\left(\sigma_j^{0,\mathrm{mod}} - \sigma_j^{0,\mathrm{obs}}\right)^2}, \tag{27}$$

$$\mathrm{MAE} = \frac{1}{N}\sum_{j=1}^{N}\left|\sigma_j^{0,\mathrm{mod}} - \sigma_j^{0,\mathrm{obs}}\right|, \tag{28}$$

and

$$\mathrm{Bias} = \frac{1}{N}\sum_{j=1}^{N}\left(\sigma_j^{0,\mathrm{mod}} - \sigma_j^{0,\mathrm{obs}}\right), \tag{29}$$

where N is the number of evaluated pixels.

Figure 6 compares observed and reconstructed backscatter coefficients. Figure 6a–e show results for the model-specific retrievable pixels, whereas Figure 6f–j show results for the 342 pixels retrievable under all four roughness assumptions. The dashed line denotes the one-to-one relationship.

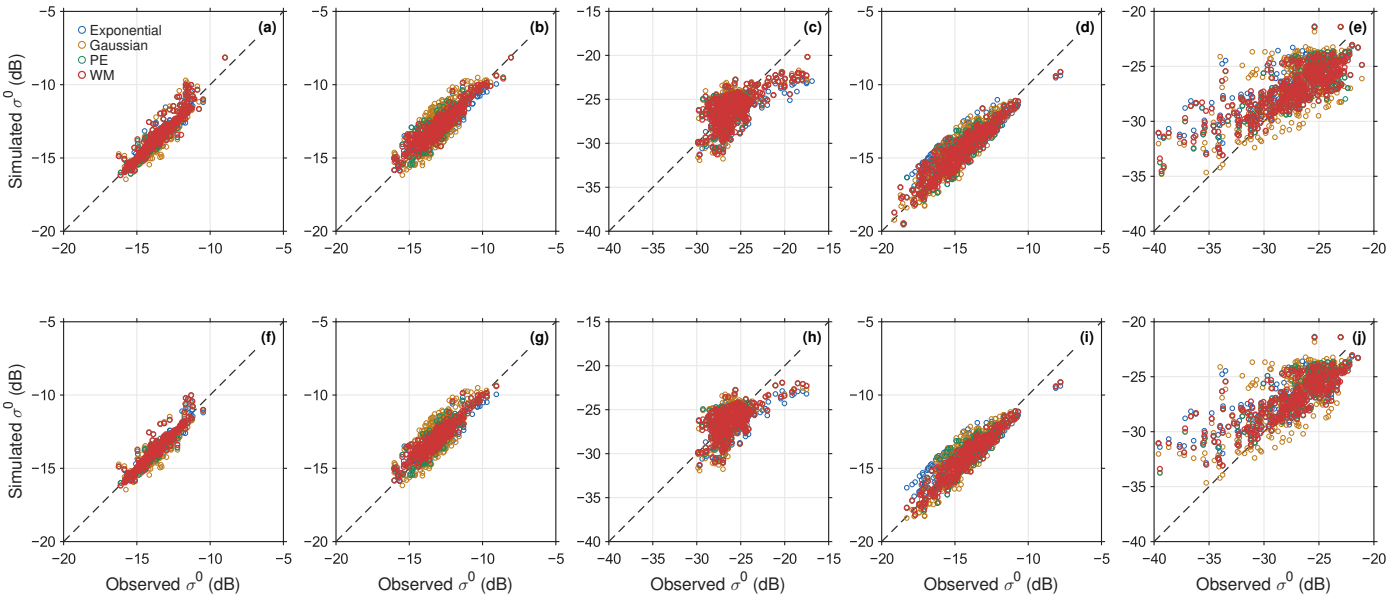


Figure 6. Comparison of observed and reconstructed backscatter coefficients for the exponential, Gaussian, PE, and WM roughness assumptions: (**a**–**e**) model-specific retrievable pixels and (**f**–**j**) the 342 pixels retrievable by all four models. From left to right, the channels are RADARSAT-2 HH, VV, and HV, followed by Sentinel-1 VV and VH. The dashed line denotes the one-to-one relationship.

The co-polarized channels, RADARSAT-2 HH and VV and Sentinel-1 VV, are more closely distributed around the one-to-one line than the cross-polarized channels. The HV and VH channels show greater dispersion, consistent with their stronger sensitivity to small scale roughness, residual vegetation, sensor noise, and limitations of the empirical cross-polarized scattering model. Although the same Oh-type formulation is used for the cross-polarized channels in all experiments, reconstructed values differ among roughness models because the jointly retrieved roughness and soil moisture parameters are constrained by the covariance-dependent co-polarized mEAIEM simulations.

Table 3 summarizes reconstruction statistics for the model-specific retrievable pixels. The WM model is evaluated over 425 pixels, compared with 384, 387, and 423 pixels for the exponential, Gaussian, and PE models, respectively. It therefore provides the widest spatial coverage while generally yielding the strongest reconstruction performance.

Across the five channels, the WM model yields the lowest MAE for RADARSAT-2 HH, VV, and HV, and Sentinel-1 VV. It also gives the highest correlation coefficient for RADARSAT-2 VV and HV, and Sentinel-1 VV and VH. For Sentinel-1 VH, the PE model produces the lowest RMSE (2.212 dB) and MAE (1.616 dB), whereas the WM model has a slightly higher correlation coefficient ($R = 0.806$, compared with $R = 0.803$). For RADARSAT-2 HH, the exponential model has a slightly lower RMSE than the WM model (0.333 dB versus 0.388 dB); however, the WM model has the lowest MAE (0.222 dB) and a comparable correlation coefficient (0.947 versus 0.948). Overall, the WM model combines the largest spatial coverage with lower reconstruction errors and higher correlation for most channels.

Table 3. Backscatter reconstruction statistics for model-specific retrievable pixels.

Polarization	Roughness Assumption	Pixels	RMSE (dB)	95% CI of RMSE (dB)	MAE (dB)	Bias (dB)	R
RADARSAT-2 HH	Exponential	384	0.333	[0.279, 0.371]	0.230	−0.079	0.948
	Gaussian	387	0.513	[0.433, 0.571]	0.373	−0.125	0.917
	Powered Exponential	423	0.391	[0.303, 0.440]	0.235	0.017	0.947
	Whittle–Matérn	425	0.388	[0.301, 0.441]	0.222	0.026	0.947
RADARSAT-2 VV	Exponential	384	0.605	[0.550, 0.665]	0.479	0.154	0.868
	Gaussian	387	0.873	[0.812, 0.930]	0.730	0.266	0.820
	Powered Exponential	423	0.577	[0.523, 0.629]	0.450	0.205	0.901
	Whittle–Matérn	425	0.505	[0.451, 0.551]	0.386	0.186	0.926
RADARSAT-2 HV	Exponential	384	1.773	[1.547, 1.974]	1.355	−0.382	0.553
	Gaussian	387	1.762	[1.540, 1.887]	1.385	−0.208	0.653
	Powered Exponential	423	1.681	[1.469, 1.797]	1.290	−0.223	0.659
	Whittle–Matérn	425	1.669	[1.471, 1.792]	1.285	−0.293	0.670
Sentinel-1 VV	Exponential	384	0.837	[0.764, 0.905]	0.672	0.208	0.868
	Gaussian	387	0.792	[0.733, 0.852]	0.648	0.120	0.902
	Powered Exponential	423	0.689	[0.615, 0.741]	0.542	0.021	0.920
	Whittle–Matérn	425	0.624	[0.550, 0.678]	0.481	0.028	0.935
Sentinel-1 VH	Exponential	384	2.354	[2.018, 2.724]	1.695	0.688	0.777
	Gaussian	387	2.460	[2.159, 2.796]	1.794	0.463	0.704
	Powered Exponential	423	2.212	[1.936, 2.522]	1.616	0.309	0.803
	Whittle–Matérn	425	2.263	[1.966, 2.593]	1.647	0.378	0.806

Because the models are evaluated over different numbers of retrievable pixels, the preceding comparison reflects both reconstruction quality and spatial coverage. To isolate reconstruction differences under identical pixel conditions, the analysis is repeated for the common subset of 342 pixels.

As shown in Table 4, the WM model produces the lowest MAE for all channels except Sentinel-1 VH, and it provides the lowest RMSE and highest correlation coefficient for most channels. The largest improvement occurs for Sentinel-1 VV, where the WM model reduces RMSE to 0.501 dB, compared with 0.820 dB, 0.786 dB, and 0.606 dB for the exponential, Gaussian, and PE models, respectively. It also gives the lowest MAE (0.399 dB) and the highest correlation coefficient ($R = 0.951$). For Sentinel-1 VH, the PE model performs best,

with an RMSE of 2.089 dB, an MAE of 1.471 dB, and $R = 0.823$. The corresponding WM values are 2.128 dB, 1.497 dB, and 0.818. For RADARSAT-2 *HH*, the exponential and WM models perform similarly. The exponential model has a slightly lower RMSE (0.314 dB versus 0.332 dB), whereas the WM model has the lowest MAE (0.184 dB) and the smallest absolute bias (−0.011 dB). Overall, the WM model improves multi-channel reconstruction while remaining competitive for RADARSAT-2 *HH* and Sentinel-1 *VH*.

Table 4. Backscatter reconstruction statistics for the 342 pixels retrievable by all four models.

Polarization	Roughness Assumption	Pixels	RMSE (dB)	95% CI of RMSE (dB)	MAE (dB)	Bias (dB)	*R*
RADARSAT-2 *HH*	Exponential	342	0.314	[0.266, 0.340]	0.219	−0.094	0.955
	Gaussian	342	0.468	[0.405, 0.510]	0.348	−0.193	0.912
	Powered Exponential	342	0.346	[0.279, 0.395]	0.202	−0.029	0.945
	Whittle–Matérn	342	0.332	[0.264, 0.386]	0.184	−0.011	0.948
RADARSAT-2 *VV*	Exponential	342	0.576	[0.524, 0.623]	0.461	0.114	0.874
	Gaussian	342	0.891	[0.821, 0.946]	0.750	0.272	0.792
	Powered Exponential	342	0.553	[0.497, 0.593]	0.438	0.202	0.899
	Whittle–Matérn	342	0.473	[0.415, 0.512]	0.358	0.192	0.927
RADARSAT-2 *HV*	Exponential	342	1.634	[1.442, 1.777]	1.267	−0.336	0.564
	Gaussian	342	1.660	[1.471, 1.779]	1.312	−0.141	0.578
	Powered Exponential	342	1.550	[1.370, 1.673]	1.194	−0.176	0.608
	Whittle–Matérn	342	1.514	[1.341, 1.645]	1.172	−0.216	0.623
Sentinel-1 *VV*	Exponential	342	0.820	[0.744, 0.887]	0.653	0.198	0.871
	Gaussian	342	0.786	[0.722, 0.848]	0.641	0.069	0.885
	Powered Exponential	342	0.606	[0.544, 0.653]	0.479	−0.070	0.927
	Whittle–Matérn	342	0.501	[0.452, 0.537]	0.399	−0.072	0.951
Sentinel-1 *VH*	Exponential	342	2.247	[1.863, 2.637]	1.577	0.779	0.802
	Gaussian	342	2.404	[2.077, 2.788]	1.716	0.687	0.730
	Powered Exponential	342	2.089	[1.758, 2.453]	1.471	0.584	0.823
	Whittle–Matérn	342	2.128	[1.801, 2.499]	1.497	0.552	0.818

3.6. Effect of Sample Size

To further assess the effect of sample size, we use the 342 pixels common to all four models as the sampling population. Random samples are drawn without replacement, with sample sizes ranging from 50 to 342 pixels. For each sample size, the procedure is repeated 1000 times, and the mean and standard deviation of the reconstruction RMSE are calculated for each model and polarization channel. The results are shown in Figures 7 and 8, which present the RMSE mean and standard deviation, respectively, as functions of sample size.

The mean RMSE remains generally stable as the sample size increases, and the relative performance of the four models is unchanged across the polarization channels (Figure 7). In contrast, the RMSE standard deviation decreases markedly with increasing sample size. Except for the RADARSAT-2 *HH* channel, WM generally shows the smallest RMSE standard deviation across channels and sample sizes (Figure 8). This indicates that WM produces the most stable reconstruction performance under different random subsets of pixels and is therefore less sensitive to sample composition.

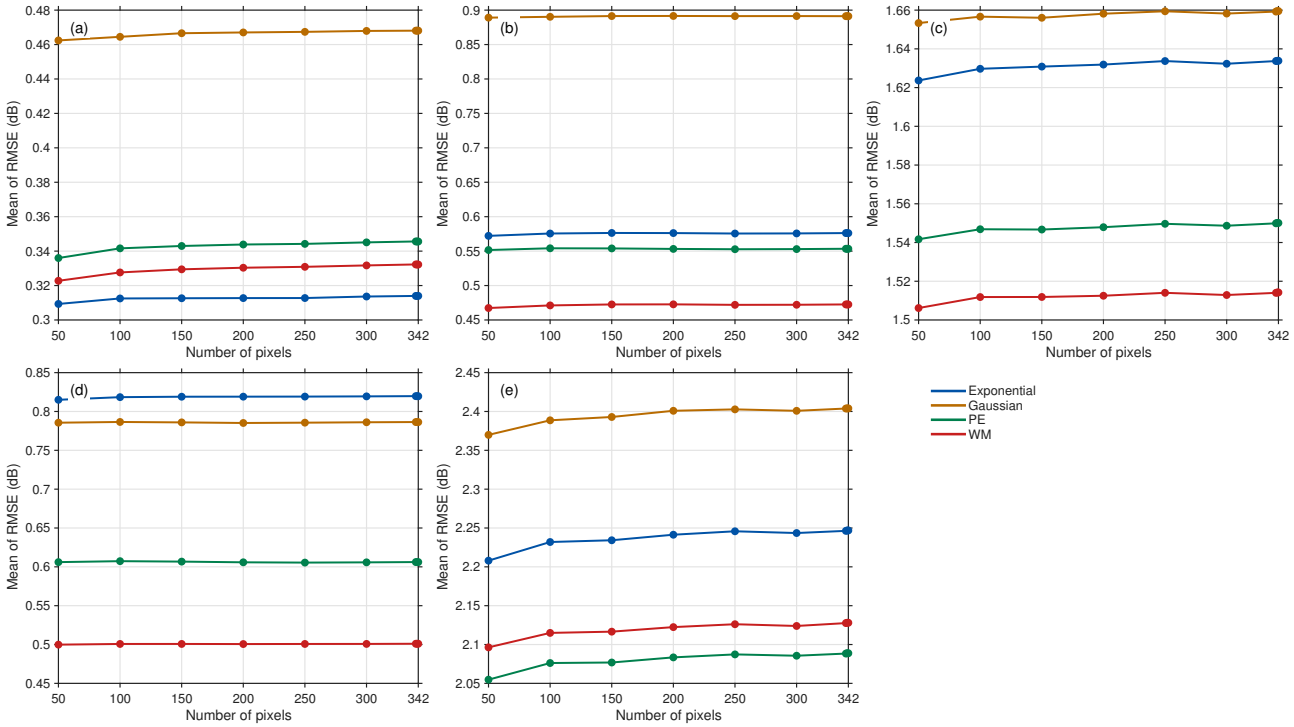


Figure 7. Effect of sample size on the mean backscatter reconstruction RMSE for the different roughness models: (**a**) RADARSAT-2 *HH*, (**b**) RADARSAT-2 *VV*, (**c**) RADARSAT-2 *HV*, (**d**) Sentinel-1 *VV*, and (**e**) Sentinel-1 *VH*.

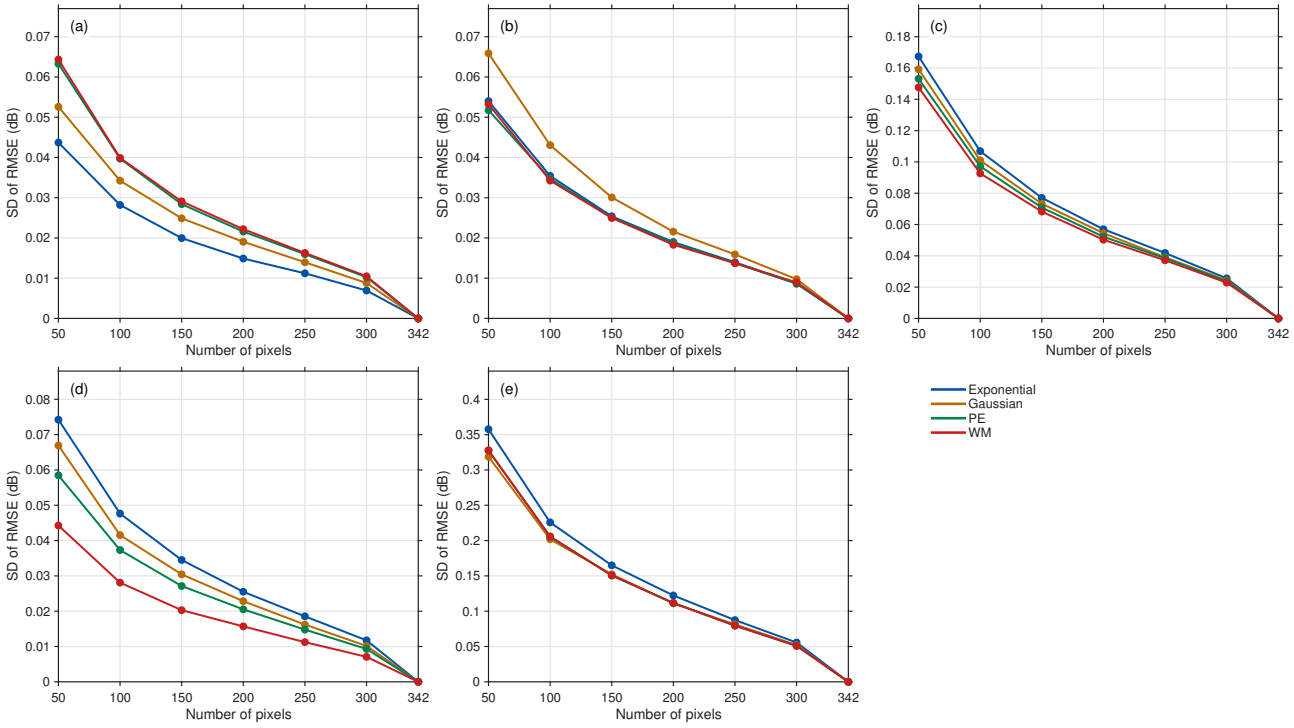


Figure 8. Effect of sample size on the standard deviation of backscatter reconstruction RMSE for the different roughness models: (**a**) RADARSAT-2 *HH*, (**b**) RADARSAT-2 *VV*, (**c**) RADARSAT-2 *HV*, (**d**) Sentinel-1 *VV*, and (**e**) Sentinel-1 *VH*.

The rapid decrease in the RMSE standard deviation with increasing sampling size (Figure 8) is primarily attributed to the finite-population correction associated with sampling without replacement from the fixed set of 342 common pixels. To isolate the effect of sampling size, the RMSE standard deviation is normalized by its value at $n = 300$. The corresponding normalized RMSE standard deviation is $\frac{SD_n}{SD_{300}} = \sqrt{\frac{(N-n)/n}{(N-N_{\text{ref}})/N_{\text{ref}}}}$, with $N = 342$ and $N_{\text{ref}} = 300$. This theoretical ratio combines the usual $1/\sqrt{n}$ dependence with the finite population correction (FPC) [31,32]. As n approaches 342, the sampling variability approaches zero because the sample increasingly represents the complete finite population. Figure 9 compares the normalized standard deviation obtained from the five polarization channels with the theoretical ratio. The results show very good agreement across all channels and sampling sizes. Unless stated otherwise, all subsequent analyses used the 342 common pixels.

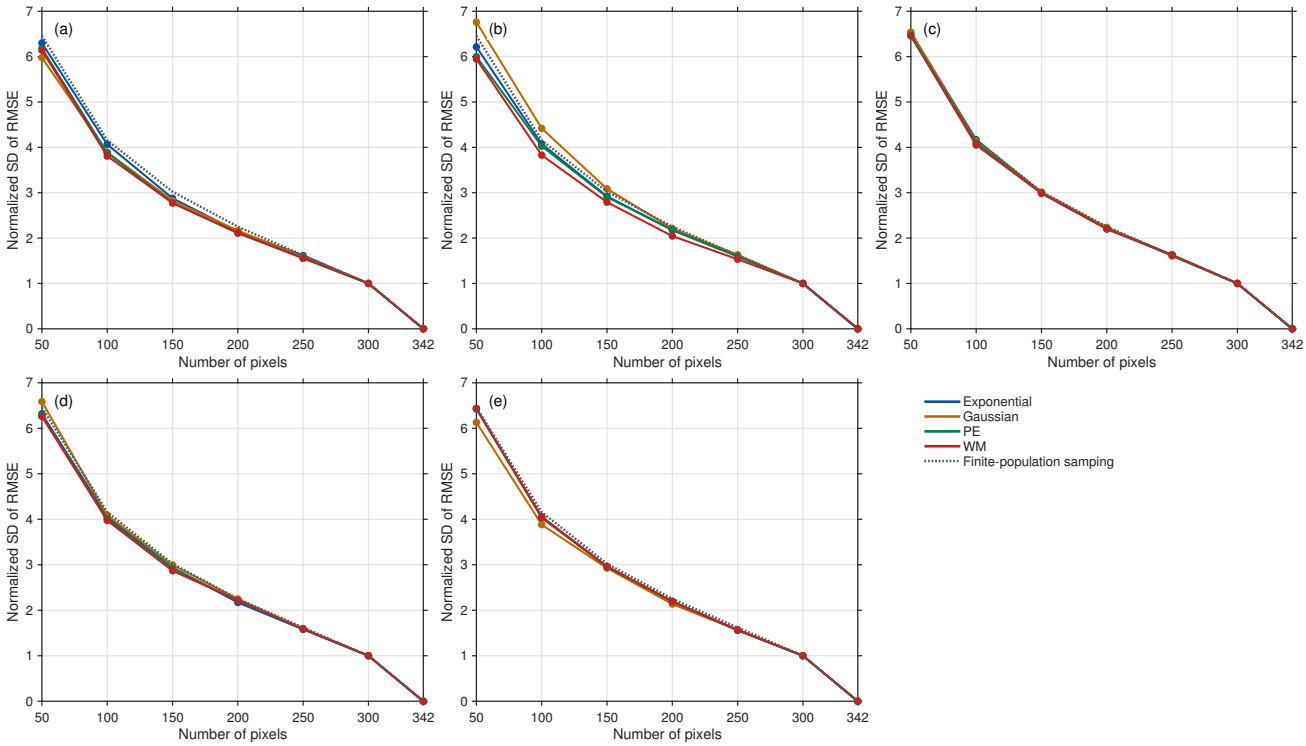


Figure 9. Effect of sample size on the normalized standard deviation of backscatter reconstruction RMSE for the different roughness models: (**a**) RADARSAT-2 *HH*, (**b**) RADARSAT-2 *VV*, (**c**) RADARSAT-2 *HV*, (**d**) Sentinel-1 *VV*, and (**e**) Sentinel-1 *VH*.

3.7. Estimated PE Shape Parameter and WM Smoothness Parameter

The PE inversion provides pixel-wise estimates of the shape parameter α, which controls the form of the surface correlation function and its associated roughness spectrum. Similarly, the WM inversion retrieves the pixel-wise smoothness parameter ν, which governs the correlation function shape and associated roughness spectrum used in the co-polarized backscatter simulation. Figure 10 shows the spatial distributions of α and ν, while Figure 11 presents their corresponding histograms. Table 5 provides the associated numerical statistics.

The PE shape parameter α shows substantial spatial variability across the study area. Many pixels have values near $\alpha = 1$, indicating correlation structures close to the exponential form. Thus, although exponential-like behavior is common, the correlation function shape varies locally and is not fully represented by a single fixed exponential or Gaussian model.

The retrieved ν values also vary substantially across the study area. Low values dominate much of the scene, whereas moderate and high values occur mainly in localized patches and linear features. This pattern is also evident in the histogram (Figure 11).

A small proportion of estimates accumulates at $\nu = 10$, the upper bound imposed during inversion. This represents a bound-constrained retrieval artifact rather than a resolved concentration of surfaces with exactly $\nu = 10$. Increasing the upper bound could refine estimates of ν, and potentially the associated roughness parameters, for these pixels. It may also modestly improve backscatter reconstruction where the optimum lies beyond the current search range. However, because only a small fraction of pixels reaches the bound, expanding the search space would increase computational cost with limited overall benefit. The adopted upper bound therefore provides a practical balance between parameter space coverage and computational efficiency.

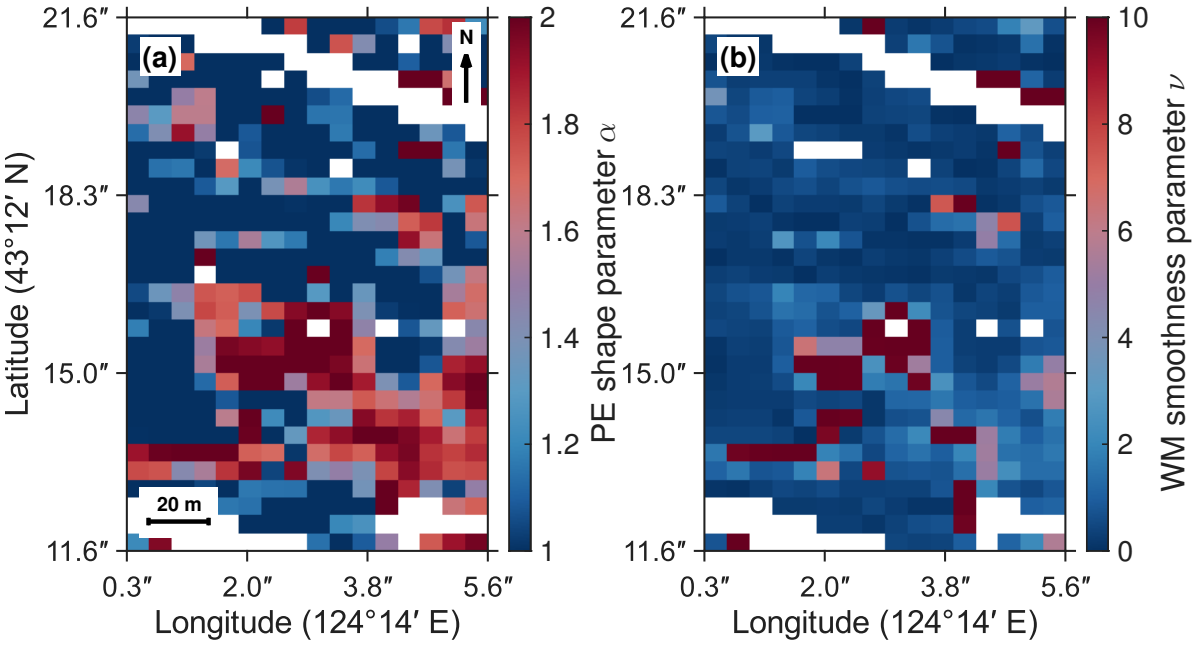


Figure 10. Pixel-wise estimates of (**a**) the PE shape parameter α and (**b**) the WM smoothness parameter ν.

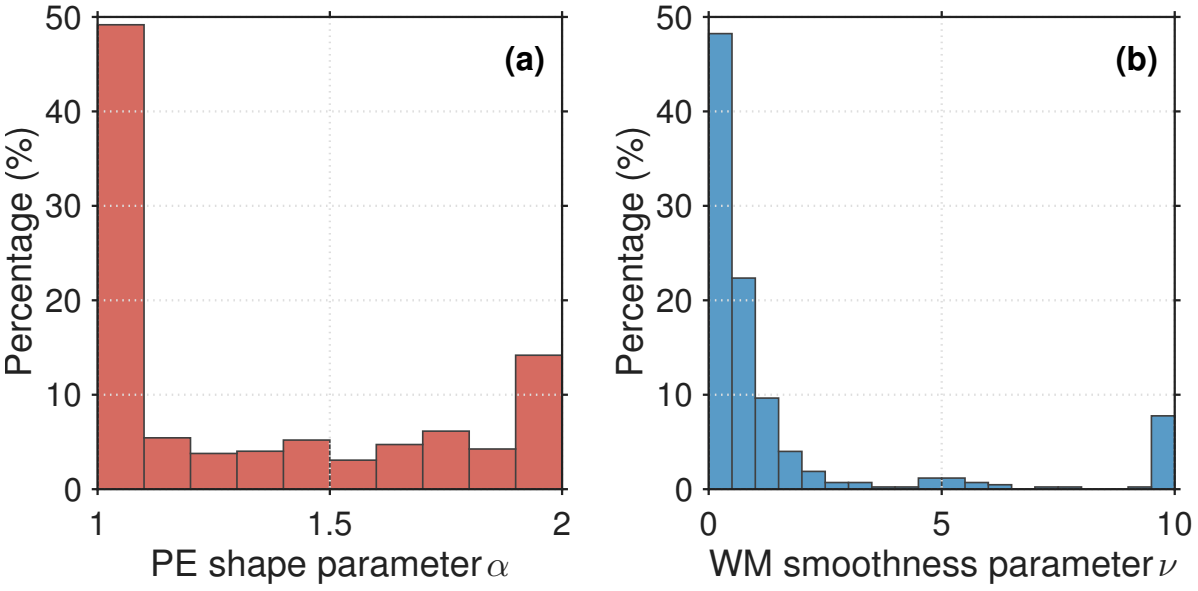


Figure 11. Histograms of the pixel-wise estimates of (**a**) the PE shape parameter α and (**b**) the WM smoothness parameter ν.

Table 5. Binned distributions of the pixel-wise estimates of the PE shape parameter α and the WM smoothness parameter ν.

Powered Exponential (α, $N = 423$)			Whittle–Matérn (ν, $N = 425$)					
Range	**Pixels**	**Percentage (%)**	**Range**	**Pixels**	**Percentage (%)**	**Range**	**Pixels**	**Percentage (%)**
1.0–1.1	208	49.17	0.0–0.5	205	48.24	5.0–5.5	5	1.18
1.1–1.2	23	5.44	0.5–1.0	95	22.35	5.5–6.0	3	0.71
1.2–1.3	16	3.78	1.0–1.5	41	9.65	6.0–6.5	2	0.47
1.3–1.4	17	4.02	1.5–2.0	17	4.00	6.5–7.0	0	0.00
1.4–1.5	22	5.20	2.0–2.5	8	1.88	7.0–7.5	1	0.24
1.5–1.6	13	3.07	2.5–3.0	3	0.71	7.5–8.0	1	0.24
1.6–1.7	20	4.73	3.0–3.5	3	0.71	8.0–8.5	0	0.00
1.7–1.8	26	6.15	3.5–4.0	1	0.24	8.5–9.0	0	0.00
1.8–1.9	18	4.26	4.0–4.5	1	0.24	9.0–9.5	1	0.24
1.9–2.0	60	14.18	4.5–5.0	5	1.18	9.5–10.0	33	7.76

3.8. Estimated Roughness Parameters

Figure 12 shows the pixel-wise estimates of rms height s and correlation length ℓ obtained with the exponential, Gaussian, PE, and WM roughness models. The WM model provides the broadest spatial coverage because fewer pixels are excluded by the model-consistency criterion.

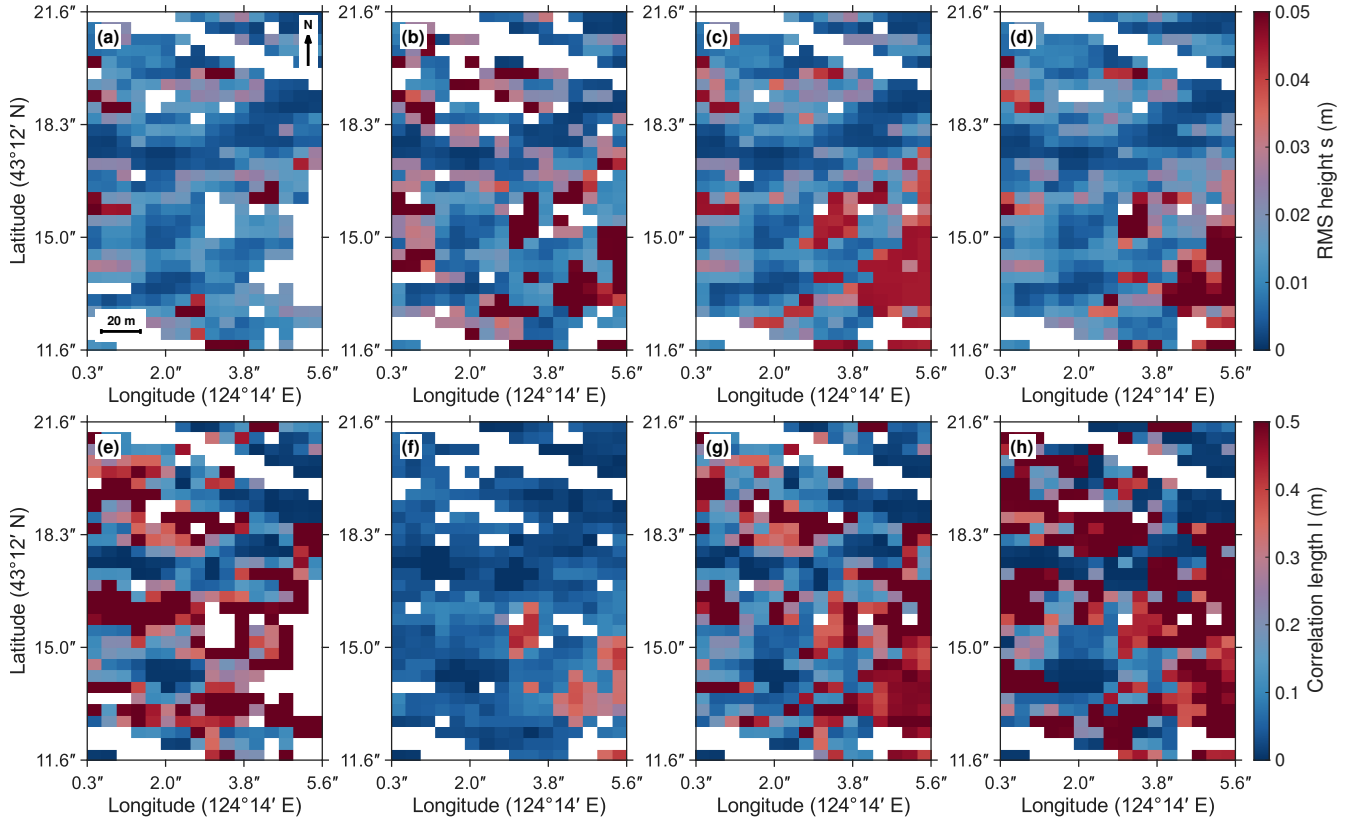


Figure 12. Pixel-wise estimates of roughness parameters: (**a**–**d**) rms height s for the exponential, Gaussian, PE, and WM models, respectively; and (**e**–**h**) correlation length ℓ for the exponential, Gaussian, PE, and WM models, respectively.

The exponential, PE, and WM models generally retrieve lower rms heights and broader distributions of correlation length, with different patterns of locally elevated values in several parts of the study area. In contrast, the Gaussian model tends to produce larger rms heights and shorter correlation lengths. These differences reflect the coupled roles of rms height, correlation length, and correlation function shape in determining the simulated roughness spectrum.

3.9. Retrieved Soil Moisture Maps

Figure 13 shows the pixel-wise volumetric soil moisture estimates obtained using the exponential, Gaussian, PE, and WM roughness models. Pixels that fail the co-polarized model-consistency criterion are masked.

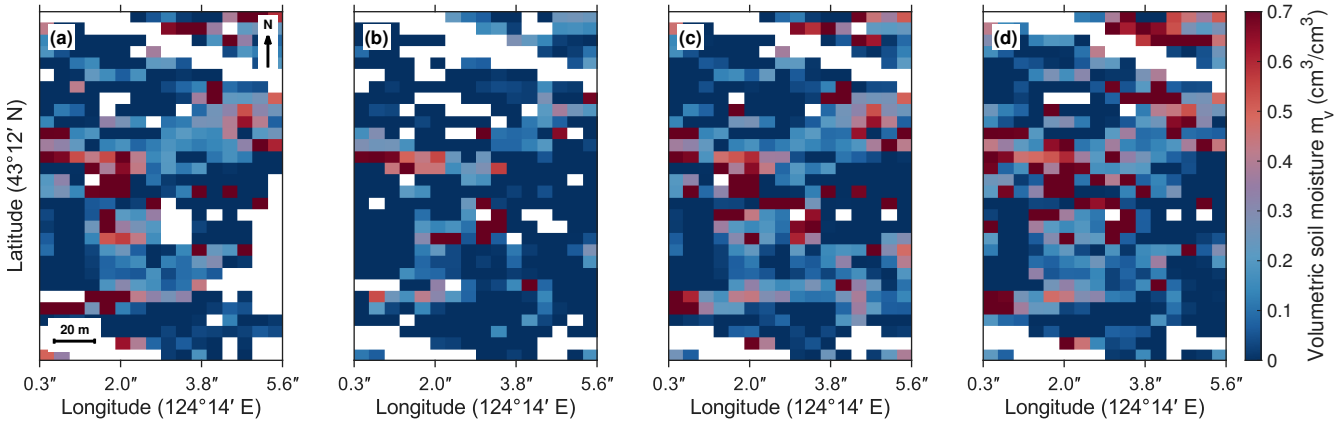


Figure 13. Pixel-wise retrieved volumetric soil moisture m_v using (**a**) exponential, (**b**) Gaussian, (**c**) PE, and (**d**) WM roughness assumptions. White pixels denote blind inversion points or pixels masked by the co-polarized model-consistency criterion.

The four roughness assumptions produce distinct soil moisture patterns and spatial coverages. The exponential model retrieves a relatively broad range of values, including localized estimates near the upper bound of the prescribed search interval. The Gaussian model generally produces lower soil moisture values. The PE model also yields a broad range of estimates, but with more complete coverage and greater spatial continuity than the exponential and Gaussian models. The WM model provides the broadest coverage and most spatially continuous map while preserving coherent field scale patterns.

Mean retrieved soil moisture values are compared with concurrent SMAP Level-4 surface soil moisture data and observations from five nearby in situ stations. The comparison is conducted for both model-specific retrievable pixels and the common retrievable subset. The latter isolates differences attributable to unequal spatial coverage among the models. The mean difference is defined as

$$\Delta\overline{m}_v = \overline{m}_{v,\mathrm{mod}} - \overline{m}_{v,\mathrm{ref}}, \tag{30}$$

where $\overline{m}_{v,\mathrm{mod}}$ and $\overline{m}_{v,\mathrm{ref}}$ are the mean model-retrieved and reference soil moisture values, respectively. Negative values of $\Delta\overline{m}_v$ indicate underestimation relative to the reference mean.

Table 6 summarizes the results. For the model-specific pixel sets, all models underestimate the reference soil moisture, whereas the WM model consistently has the smallest absolute mean difference. Relative to SMAP, the mean differences are -0.045 cm^3 cm^{-3}, -0.138 cm^3 cm^{-3}, -0.047 cm^3 cm^{-3}, and -0.013 cm^3 cm^{-3} for the exponential, Gaussian, PE, and WM models, respectively.

The common pixel analysis gives the same ranking. The Gaussian model has the largest negative bias, the exponential and PE models show intermediate differences, and the WM

model remains closest to each reference dataset. For SMAP, the WM mean difference is -0.009 cm^3 cm^{-3} over the common retrievable pixels.

Because SMAP has a much coarser spatial support than the SAR retrievals and the station measurements are point observations, these comparisons assess regional mean consistency rather than pixel scale accuracy. Nevertheless, for both the model-specific and common pixel comparisons, WM retrievals are consistently closer to the reference means than those obtained using the fixed form models.

Table 6. Mean differences $\Delta\overline{m}_v = \overline{m}_{v,\mathrm{mod}} - \overline{m}_{v,\mathrm{ref}}$ between retrieved and reference volumetric soil moisture, in cm^3 cm^{-3}. Negative values indicate that the model-retrieved mean is lower than the reference mean.

Reference	$\overline{m}_{v,\mathrm{ref}}$	Model-Specific Retrievable Pixels				Common Retrievable Pixels			
		Exponential	Gaussian	PE	WM	Exponential	Gaussian	PE	WM
SMAP	0.220	−0.045	−0.138	−0.047	−0.013	−0.043	−0.147	−0.054	−0.009
Site 54154	0.275	−0.100	−0.192	−0.101	−0.067	−0.097	−0.201	−0.108	−0.064
Site E4055	0.221	−0.046	−0.138	−0.048	−0.014	−0.044	−0.146	−0.055	−0.010
Site E0131	0.302	−0.126	−0.219	−0.129	−0.094	−0.124	−0.228	−0.135	−0.091
Site E0134	0.374	−0.199	−0.291	−0.200	−0.166	−0.197	−0.300	−0.208	−0.164
Site L7532	0.332	−0.158	−0.250	−0.159	−0.125	−0.155	−0.259	−0.166	−0.122

4. Discussion

4.1. Covariance Representation and Inversion Feasibility

Agricultural surface roughness is scale dependent. The covariance function used in a scattering model is therefore not a neutral choice. Statistics derived from short field profiles may not represent the spatial separations that contribute most to SAR scattering, and departures from the assumed covariance can strongly affect simulated backscatter [33]. Such mismatch cannot always be absorbed by adjusting rms height s and a single correlation length ℓ within fixed exponential or Gaussian covariance families.

The WM–mEAIEM formulation [16] addresses this limitation by representing roughness as a Gaussian–Gamma scale mixture. Instead of imposing one effective correlation scale, WM combines a continuum of Gaussian scales, with their relative weights controlled by ℓ and ν. This changes the distribution of roughness spectral energy over the wavenumber range relevant to scattering. WM should therefore be interpreted as a multiscale roughness representation, not simply as a model with one additional fitting parameter.

The inversion results support the importance of this distinction. Under the same parameter bounds, residual tolerance, and optimization settings, the fixed exponential and Gaussian models produced blind point ratios of about 12%, whereas PE and WM reduced this fraction to about 3% (Table 2). Thus, a substantial fraction of the observed multi-sensor co-polarized vectors could not be reproduced by the fixed covariance families within the prescribed inversion domain. When the covariance structure is inadequate, the inversion can compensate through changes in s, ℓ, and m_v; blind points occur when this compensation is insufficient. A lower blind point ratio therefore indicates improved inversion feasibility, but not necessarily higher retrieval accuracy.

PE provides a useful comparison because it also relaxes the fixed covariance shape. Its low blind point ratio indicates that noncanonical covariance structures are needed under the present inversion configuration. PE and WM, however, introduce flexibility in different ways. PE modifies the covariance decay and the associated spectral shape, whereas WM changes the mixture of effective correlation scales. Figure 4 shows that WM provides closer reconstruction of the observed five channel backscatter for a larger proportion of

pixels. Figure 5 demonstrates that WM minimizes both the number and spatial extent of blind pixels, producing a more continuous model-consistent domain. The results in Figure 8 further indicate that WM is generally less sensitive to sample composition. Because PE and WM retrieve the same number of roughness shape parameters, their different performance over common pixels cannot be attributed to parameter count alone. The WM representation is more consistent with the scale-dependent roughness characteristics of agricultural surfaces [12] than a formulation based solely on the PE shape parameter α. The superior performance of WM across reconstruction accuracy, inversion feasibility, and sampling stability supports the value of its multiscale covariance representation.

These findings extend earlier profile-based and forward modeling studies to the joint inversion of real SAR observations. For example, Zribi et al. [18] found that the powered exponential covariance better described measured agricultural profiles than exponential or Gaussian forms and improved backscatter simulations under moderate- to high-moisture conditions. In this study, all covariance formulations were tested within the same scattering framework and with the same inversion settings. Covariance representation is therefore the principal modeled difference among the tested retrievals. The physical meaning and pixel-scale validity of the retrieved shape parameters, however, still require independent measurements of surface roughness and soil moisture.

4.2. Interpretation and Limits of the Retrieved Shape Parameters

The spatial variability of ν shown in Figures 10 and 11, together with Table 5, indicates that roughness correlation structure is not uniform across the study area. This helps explain why fixed exponential and Gaussian covariance functions do not perform equally well for all pixels. The result is consistent with the field-scale observations of Davidson et al. [12], who showed that the apparent correlation structure of agricultural surfaces can vary with profile length. The spatially varying ν values retrieved here may likewise reflect multiscale roughness within the radar resolution cell.

The retrieved shape parameters should be interpreted as effective indicators of covariance structure, rather than direct measurements of physical roughness features. Their main role here is to diagnose whether the observations favor covariance forms outside the canonical exponential and Gaussian limits.

For PE, approximately 49% of estimates fell between $\alpha = 1.0$ and 1.1 (bin width 0.1). For WM, approximately 48% fell between $\nu = 0$ and 0.5 (bin width 0.5) (Figure 11). Under the parameterizations used here, these ranges lie near the exponential end of the two covariance families. This is consistent with the common use of exponential covariance functions for agricultural rough surfaces.

The Gaussian limit accounted for a smaller fraction of the retrievals. About 14% of PE estimates fell between $\alpha = 1.9$ and 2.0, and about 8% of WM estimates fell between $\nu = 9.5$ and 10. Because $\alpha = 2$ and $\nu = 10$ were upper bounds, these accumulations may partly reflect bound-constrained solutions rather than truly Gaussian roughness. The fraction of pixels physically close to the Gaussian limit is therefore likely smaller than the upper-bin percentages suggest.

More importantly, many pixels were not concentrated near either limiting form: more than 37% for PE and more than 44% for WM (Figure 11). These pixels required covariance structures that could not be represented by varying s and ℓ within fixed exponential or Gaussian families. This result is consistent with profile-based evidence that covariance shape varies with tillage, rainfall-driven surface evolution, and roughness condition [18].

The retrieved shape parameters remain model dependent. They are estimated jointly with s, ℓ, and m_v from multi-sensor backscatter and may be affected by viewing geometry, measurement support, observational uncertainty, and limitations of the scattering

model [33]. For PE, α may be statistically coupled with rms height. For WM, spatial variation in ν indicates that the mixture of effective correlation scales required by the observations varied across the scene. By allowing the covariance shape to vary, WM can represent local roughness spectra that would otherwise require compensating changes in rms height and correlation length under fixed exponential or Gaussian assumptions. This flexibility reduces the occurrence of blind points and contributes to the broader spatial coverage of the WM retrieval.

The retrieved correlation lengths should be interpreted cautiously. Agricultural surface correlation length is scale dependent and varies with tillage condition, profile length, and measurement resolution [12]. Because the present retrievals are based on SAR observations with pixel dimensions of several meters or more, the estimated correlation lengths represent effective roughness properties at the radar scale rather than unique physical dimensions of surface features.

Several studies have calibrated an effective correlation length, which keeps the covariance family fixed and adjusts ℓ to account for measurement uncertainty or IEM limitations [5,34,35]. Here, correlation scale and covariance shape were retrieved jointly. The lower blind point ratios of PE and WM suggest that adjusting ℓ alone within a fixed exponential or Gaussian covariance was not sufficient to resolve the observed mismatch.

4.3. Parameter Compensation and Soil Moisture Consistency

The covariance assumption also affected how backscatter mismatch was allocated among roughness and soil moisture parameters. The four models produced systematically different estimates of s, ℓ, and m_v (Figures 12 and 13). The Gaussian model retrieved relatively large rms heights and short correlation lengths and had a mean difference from SMAP of -0.138 cm^3 cm^{-3} (Table 6). In contrast, the exponential model retrieved soil moisture near the upper bound in parts of the scene. These contrasts are consistent with parameter compensation in a nonunique SAR inversion, where similar backscatter values can result from different combinations of roughness and soil moisture parameters [36].

Prior information and covariance flexibility address different aspects of this problem. Prior information restricts the admissible combinations of s, ℓ, and m_v [36]. Covariance flexibility changes the roughness representation in the forward model. PE relaxes the fixed covariance shape, whereas WM represents roughness through a distribution of effective correlation scales. The lower blind point ratios of PE and WM indicate that these formulations more often produced feasible solutions within the prescribed bounds. This suggests that part of the observed backscatter variation could be represented through covariance structure rather than being transferred entirely to s, ℓ, or m_v.

Improved feasibility, however, did not automatically lead to better soil moisture consistency. PE reduced the blind point ratio but had a mean difference from SMAP of -0.054 cm^3 cm^{-3}, larger in magnitude than that of the exponential model (-0.043 cm^3 cm^{-3}). WM showed the closest scene scale mean agreement with SMAP over the common-pixel subset (-0.009 cm^3 cm^{-3}). Together with its low blind point ratio and stronger co-polarized reconstruction, this result is consistent with reduced transfer of covariance model mismatch into the WM soil moisture estimate.

The SMAP comparison should be treated as a scene scale consistency check, not as pixel-scale validation. Differences in spatial support between SMAP and SAR, and possible cancellation of local errors in the mean difference, prevent a direct assessment of absolute soil moisture accuracy. Such an assessment requires spatially distributed and temporally matched field measurements of both soil moisture and surface roughness.

4.4. Channel-Dependent Evidence

The reconstruction statistics in Table 3 vary substantially among polarization channels. In general, the co-polarized channels, RADARSAT-2 HH and VV and Sentinel-1 VV, show lower errors and higher correlation coefficients than the cross-polarized channels, RADARSAT-2 HV and Sentinel-1 VH. For example, the lowest RMSE values for the co-polarized channels range from 0.333 to 0.624 dB, compared with 1.669 dB for RADARSAT-2 HV and 2.212 dB for Sentinel-1 VH. This difference is likely related to the distinct scattering characteristics of the polarization channels. Co-polarized backscatter is generally more closely associated with surface scattering, whereas cross-polarized backscatter is more susceptible to volume scattering, depolarization, and measurement noise. The cross-polarized channels therefore exhibit greater reconstruction uncertainty.

The common pixel analysis in Table 4 addresses a different question from the blind point analysis. It evaluates how well each covariance formulation reconstructs the individual SAR channels after a successful retrieval has been obtained for all four models.

The strongest evidence appears in the VV channels. For RADARSAT-2 VV, WM achieved the lowest RMSE (0.473 dB) and the highest correlation ($R = 0.927$). For Sentinel-1 VV, WM also produced the lowest RMSE (0.501 dB), compared with 0.606 dB for PE, 0.820 dB for the exponential model, and 0.786 dB for the Gaussian model. Because mEAIEM uses the roughness spectrum derived from the covariance function to simulate co-polarized scattering, the consistent improvement in VV supports the interpretation that WM provides a more suitable roughness-spectrum representation for these observations.

The HH results were less uniform. For RADARSAT-2 HH, the exponential model had a slightly lower RMSE than WM (0.314 versus 0.332 dB), although WM had the lowest MAE and a near zero bias. WM is therefore not superior for every co-polarized metric. Its advantage is clearest and most consistent in the VV channels across the two sensors.

The cross-polarized channels provide weaker evidence for covariance effects. The HV/VH component was represented using an Oh-type semi-empirical model [21], which does not explicitly include covariance shape. Although WM produced the lowest RMSE for RADARSAT-2 HV and PE for Sentinel-1 VH, these differences cannot be attributed directly to the respective covariance formulations.

Taken together, the blind point statistics and the co-polarized reconstruction results show that covariance representation materially affects multi-sensor SAR inversion. The evidence is consistent with WM reducing the transfer of roughness-model mismatch into the joint retrieval of roughness and soil moisture, but it does not yet establish the physical validity of the retrieved roughness parameters.

4.5. Temporal Mismatch

The 35.5 h interval between the Sentinel-1 and RADARSAT-2 acquisitions is an inherent limitation of the multi-sensor analysis. Although no rainfall was recorded, unobserved irrigation, evaporation, or tillage may have changed near-surface soil moisture or surface roughness. If such changes occurred, the retrieved roughness and soil moisture parameters should be interpreted as effective values that reconcile the two quasi-coincident observations, rather than as instantaneous surface states at either overpass.

This uncertainty affects all covariance models because they were evaluated using the same observation pair, forward model, and inversion settings. The comparison therefore remains valid for assessing the effect of covariance specification on inversion feasibility, backscatter reconstruction, and consistency of the resulting effective estimates. The lower blind point ratios and improved co-polarized reconstruction obtained with PE and WM suggest that a more suitable covariance representation reduces sensitivity to roughness-model mismatch. However, lower residuals do not demonstrate that temporal changes

between acquisitions have been resolved, since unmodeled changes may be absorbed by compensating adjustments among roughness and soil moisture parameters. Independent near-synchronous observations of soil moisture, roughness, irrigation, and tillage would be needed to assess the physical representativeness of the retrieved parameters.

4.6. Implications and Future Work

The main implication is that covariance structure should be treated as an active part of SAR soil moisture inversion, rather than as a fixed background assumption. For the agricultural surfaces examined here, fixed exponential and Gaussian covariances left a larger fraction of observations outside the attainable inversion domain and led to stronger evidence of parameter compensation. PE and WM both improved feasibility, confirming that a more flexible covariance representation was needed.

Among the tested formulations, WM provided the most balanced performance. It combined a low blind point ratio, stronger co-polarized backscatter reconstruction, and closer scene scale agreement with SMAP. Because PE and WM use the same number of roughness-shape parameters, this behavior is consistent with an advantage of the Gaussian–Gamma scale-mixture representation rather than with parameter number alone.

Further validation is still needed. Independent, spatially distributed, and temporally matched measurements of soil moisture and two-dimensional surface roughness are required to assess pixel-scale accuracy, parameter identifiability, and the physical meaning of the retrieved shape parameters. Predictive performance should also be tested across independent acquisition dates, incidence angles, and sensor configurations [37]. Future work should consider anisotropic WM formulations for directional roughness caused by tillage and row orientation [38], and should extend the framework to vegetated fields using an appropriate vegetation-scattering model.

5. Conclusions

This study compared exponential, Gaussian, powered exponential (PE), and Whittle–Matérn (WM) roughness covariance representations in independent pixel-wise inversion of quasi-coincident RADARSAT-2 and Sentinel-1 observations over bare agricultural soil.

Roughness covariance representation affects inversion feasibility. At the prescribed co-polarized residual tolerance, the fixed exponential and Gaussian models produced blind point ratios of 12.53% and 11.85%, respectively, whereas PE and WM reduced these ratios to 3.64% and 3.19%. Fixed covariance forms therefore substantially restricted the attainable co-polarized backscatter domain, while flexible covariance representations made a large fraction of previously unretrievable observations retrievable within the same admissible parameter ranges.

WM provided the strongest overall performance across the evaluated diagnostics. On the common retrievable-pixel subset, it gave the most consistent reconstruction of the co-polarized observations, with its clearest advantage in the two VV channels, and it produced the closest scene scale agreement with SMAP, with a mean difference of -0.009 cm^3 cm^{-3}. Together with the systematic model-dependent shifts in s, ℓ, and m_v, these results provide strong evidence that covariance model mismatch can be transferred into retrieved roughness and soil moisture parameters.

The comparison between PE and WM shows that the benefit of flexible covariance modeling is not explained by parameter number alone. Both models retrieve the same number of roughness-shape parameters, but PE modifies covariance decay whereas WM represents a Gaussian–Gamma mixture of effective correlation scales. For the bare agricultural surfaces and multi-sensor retrieval setting examined here, WM therefore provides a more effective representation of the multiscale roughness spectrum controlling co-polarized scattering.

Independent, spatially matched observations of two-dimensional roughness and soil moisture are now needed to quantify pixel-scale accuracy, parameter identifiability, and the physical interpretation of the retrieved shape parameters. SMAP serves in the present analysis as a scene scale consistency benchmark rather than a pixel-scale validation reference. This limitation does not alter the central result: covariance structure materially controls inversion feasibility, co-polarized backscatter reconstruction, and the robustness of soil moisture retrieval in multi-sensor SAR inversion over bare agricultural soil.

Author Contributions: Conceptualization, Y.D.; methodology, Y.W. and Y.D.; software, Y.W.; validation, Y.W. and Y.D.; formal analysis, Y.W. and Y.D.; investigation, Y.W.; resources, Y.D.; data curation, Y.W.; writing—original draft preparation, Y.D.; writing—review and editing, Y.D.; visualization, Y.W.; supervision, Y.D.; project administration, Y.D.; funding acquisition, Y.D. All authors have read and agreed to the published version of the manuscript.

Funding: This research was funded by the National Key Research and Development Program of China under Grant 2022YFB3903503.

Institutional Review Board Statement: Not applicable.

Informed Consent Statement: Not applicable.

Data Availability Statement: Sentinel-1 and Sentinel-2 data are publicly available through the Copernicus Data Space Ecosystem (https://dataspace.copernicus.eu/). The SMAP Level-4 soil moisture data (SPL4SMGP, Version 8) are publicly available from the NASA National Snow and Ice Data Center Distributed Active Archive Center (https://doi.org/10.5067/T5RUATAQREF8). The CLDAS data are available through the China Meteorological Data Service Center (https://data.cma.cn/). The retrieval results supporting this study are available from the authors upon reasonable request.

Acknowledgments: The authors acknowledge the European Union's Copernicus program and the European Space Agency for the Sentinel-1 and Sentinel-2 data, and the NASA SMAP mission team and the NASA National Snow and Ice Data Center Distributed Active Archive Center for producing and distributing the SMAP soil moisture data. We also thank the National Meteorological Information Center of the China Meteorological Administration for providing the CLDAS data.

Conflicts of Interest: The authors declare no conflicts of interest.

Abbreviations

The following abbreviations are used in this manuscript:

SAR	Synthetic Aperture Radar
WM	Whittle–Matérn
PE	Powered Exponential
IEM	Integral Equation Model
mEAIEM	modified Extended Advanced Integral Equation Model
NDVI	Normalized Difference Vegetation Index
SMAP	Soil Moisture Active Passive
CLDAS	China Meteorological Administration Land Data Assimilation System
IW	Interferometric Wide
FPC	Finite Population Correction

References

1. Xie, Y.; Cui, G.; Zheng, K.; Tang, G. Integrating Sentinel-1 SAR and Machine Learning Models for Optimal Soil Moisture Sensor Placement at Catchment Scale. *Remote Sens*. **2025**, *17*, 2330. [CrossRef]
2. Lamichhane, M.; Mehan, S.; Mankin, K.R. Soil Moisture Prediction Using Remote Sensing and Machine Learning Algorithms: A Review on Progress, Challenges, and Opportunities. *Remote Sens*. **2025**, *17*, 2397. [CrossRef]
3. Fung, A.K.; Li, Z.; Chen, K.S. Backscattering from a randomly rough dielectric surface. *IEEE Trans. Geosci. Remote Sens*. **1992**, *30*, 356–369. [CrossRef]
4. Chakhar, A.; Hernández-López, D.; Ballesteros, R.; Moreno, M.A. Improvement of the Soil Moisture Retrieval Procedure Based on the Integration of UAV Photogrammetry and Satellite Remote Sensing Information. *Remote Sens*. **2021**, *13*, 4968. [CrossRef]

5. Wu, X. Assessment of Effective Roughness Parameters for Simulating Sentinel-1A Observation and Retrieving Soil Moisture over Sparsely Vegetated Field. *Remote Sens.* **2022**, *14*, 6020. [CrossRef]
6. Ettalbi, M.; Baghdadi, N.; Garambois, P.A.; Bazzi, H.; Ferreira, E.; Zribi, M. Soil Moisture Retrieval in Bare Agricultural Areas Using Sentinel-1 Images. *Remote Sens.* **2023**, *15*, 3502. [CrossRef]
7. Chen, K.S.; Wu, T.D.; Tsang, L.; Li, Q.; Shi, J.; Fung, A.K. Emission of rough surfaces calculated by the integral equation method with comparison to three-dimensional moment method simulations. *IEEE Trans. Geosci. Remote Sens.* **2003**, *41*, 90–101. [CrossRef]
8. Alvarez-Pérez, J.L. The IEM2M rough-surface scattering model for complex-permittivity scattering media. *Waves Random Complex Media* **2012**, *22*, 207–233. [CrossRef]
9. Du, Y. A new bistatic model for electromagnetic scattering from randomly rough surfaces. *Waves Random Complex Media* **2008**, *18*, 109–128. [CrossRef]
10. Chen, K.L.; Chen, K.S.; Li, Z.L.; Liu, Y. Extension and validation of an advanced integral equation model for bistatic scattering from rough surfaces. *Prog. Electromagn. Res.* **2015**, *152*, 59–76. [CrossRef]
11. Yang, J.; Li, Y.; Shi, J.; Du, Y. Modification of the extended advanced IEM for scattering from randomly rough surfaces. *IEEE Geosci. Remote Sens. Lett.* **2020**, *18*, 236–240. [CrossRef]
12. Davidson, M.W.; Le Toan, T.; Mattia, F.; Satalino, G.; Manninen, T.; Borgeaud, M. On the characterization of agricultural soil roughness for radar remote sensing studies. *IEEE Trans. Geosci. Remote Sens.* **2000**, *38*, 630–640. [CrossRef]
13. Stein, M.L. *Interpolation of Spatial Data: Some Theory for Kriging*; Springer Science & Business Media: New York, NY, USA, 1999.
14. Park, E.; Brorsen, B.W.; Harri, A. Using Bayesian Kriging for spatial smoothing in crop insurance rating. *Am. J. Agric. Econ.* **2019**, *101*, 330–351. [CrossRef]
15. De Iaco, S.; Posa, D.; Cappello, C.; Maggio, S. On some characteristics of Gaussian covariance functions. *Int. Stat. Rev.* **2021**, *89*, 36–53. [CrossRef]
16. Du, Y.; Wang, Y.; Shi, Z.; Li, Z. Unifying Exponential and Gaussian: Whittle-Matérn Covariance for Improved Rough Surface Characterization and Backscatter Modeling. *IEEE Trans. Geosci. Remote Sens.* **2026**, *64*, 2003715. [CrossRef]
17. Sinha, S.K.; Sirota, E.B.; Garoff, S.; Stanley, H.B. X-ray and Neutron Scattering from Rough Surfaces. *Phys. Rev. B* **1988**, *38*, 2297–2311. [CrossRef] [PubMed]
18. Zribi, M.; Baghdadi, N.; Holah, N.; Fafin, O.; Guérin, C. Evaluation of a Rough Soil Surface Description with ASAR-ENVISAT Radar Data. *Remote Sens. Environ.* **2005**, *95*, 67–76. [CrossRef]
19. Farr, T.G.; Rosen, P.A.; Caro, E.; Crippen, R.; Duren, R.; Hensley, S.; Kobrick, M.; Paller, M.; Rodriguez, E.; Roth, L.; et al. The Shuttle Radar Topography Mission. *Rev. Geophys.* **2007**, *45*, RG2004. [CrossRef]
20. Chen, J.; Chen, J.; Liao, A.; Cao, X.; Chen, L.; Chen, X.; He, C.; Han, G.; Peng, S.; Lu, M.; et al. Global land cover mapping at 30 m resolution: A POK-based operational approach. *ISPRS J. Photogramm. Remote Sens.* **2015**, *103*, 7–27. [CrossRef]
21. Oh, Y. Quantitative retrieval of soil moisture content and surface roughness from multipolarized radar observations of bare soil surfaces. *IEEE Trans. Geosci. Remote Sens.* **2004**, *42*, 596–601. [CrossRef]
22. He, B.; Xing, M.; Bai, X. A Synergistic Methodology for Soil Moisture Estimation in an Alpine Prairie Using Radar and Optical Satellite Data. *Remote Sens.* **2014**, *6*, 10966–10985. [CrossRef]
23. Baghdadi, N.; Choker, M.; Zribi, M.; El Hajj, M.; Paloscia, S.; Verhoest, N.E.C.; Lievens, H.; Baup, F.; Mattia, F. A New Empirical Model for Radar Scattering from Bare Soil Surfaces. *Remote Sens.* **2016**, *8*, 920. [CrossRef]
24. Dobson, M.C.; Ulaby, F.T.; Hallikainen, M.T.; El-Rayes, M.A. Microwave Dielectric Behavior of Wet Soil—Part II: Dielectric Mixing Models. *IEEE Trans. Geosci. Remote Sens.* **1985**, *GE-23*, 35–46. [CrossRef]
25. Jiang, H.; Shen, H.; Li, H.; Lei, F.; Gan, W.; Zhang, L. Evaluation of Multiple Downscaled Microwave Soil Moisture Products over the Central Tibetan Plateau. *Remote Sens.* **2017**, *9*, 402. [CrossRef]
26. Dann, J.; Bennett, K.E.; Bolton, W.R.; Wilson, C.J. Factors Controlling a Synthetic Aperture Radar (SAR) Derived Root-Zone Soil Moisture Product over the Seward Peninsula of Alaska. *Remote Sens.* **2022**, *14*, 4927. [CrossRef]
27. Pause, M. Soil Moisture Retrieval Using High Spatial Resolution Polarimetric L-Band Multi-Beam Radiometer (PLMR) Data at the Field Scale. Ph.D. Thesis, Ludwig-Maximilians-Universität München, Munich, Germany, 2011. [CrossRef]
28. Thoma, D.P.; Moran, M.S.; Bryant, R.; Rahman, M.; Holifield-Collins, C.D.; Skirvin, S.; Sano, E.E.; Slocum, K. Comparison of Four Models to Determine Surface Soil Moisture from C-Band Radar Imagery in a Sparsely Vegetated Semiarid Landscape. *Water Resour. Res.* **2006**, *42*, W01418. [CrossRef]
29. Zheng, X.; Li, L.; Chen, S.; Jiang, T.; Li, X.; Zhao, K. Temporal Evolution Characteristics and Prediction Methods of Spatial Correlation Function Shape of Rough Soil Surfaces. *Soil Tillage Res.* **2019**, *195*, 104417. [CrossRef]
30. Milenković, M.; Pfeifer, N.; Glira, P. Applying Terrestrial Laser Scanning for Soil Surface Roughness Assessment. *Remote Sens.* **2015**, *7*, 2007–2045. [CrossRef]
31. Cochran, W.G.; Cochran, W.G. *Sampling Techniques*; Wiley: New York, NY, USA, 1977; Volume 3.
32. Thompson, S.K. *Sampling*, 3rd ed.; John Wiley & Sons: Hoboken, NJ, USA, 2012. [CrossRef]

33. Verhoest, N.E.C.; Lievens, H.; Wagner, W.; Álvarez-Mozos, J.; Moran, M.S.; Mattia, F. On the Soil Roughness Parameterization Problem in Soil Moisture Retrieval of Bare Surfaces from Synthetic Aperture Radar. *Sensors* **2008**, *8*, 4213–4248. [CrossRef] [PubMed]
34. Álvarez-Mozos, J.; González-Audícana, M.; Casalí, J.; Larrañaga, A. Effective versus Measured Correlation Length for Radar-Based Surface Soil Moisture Retrieval. *Int. J. Remote Sens.* **2008**, *29*, 5397–5408. [CrossRef]
35. Tronquo, E.; Lievens, H.; Bouchat, J.; Defourny, P.; Baghdadi, N.; Verhoest, N.E.C. Soil Moisture Retrieval Using Multistatic L-Band SAR and Effective Roughness Modeling. *Remote Sens.* **2022**, *14*, 1650. [CrossRef]
36. Mattia, F.; Satalino, G.; Dente, L.; Pasquariello, G. Using a Priori Information to Improve Soil Moisture Retrieval from ENVISAT ASAR AP Data in Semiarid Regions. *IEEE Trans. Geosci. Remote Sens.* **2006**, *44*, 900–912. [CrossRef]
37. Balenzano, A.; Mattia, F.; Satalino, G.; Davidson, M.W.J. Dense Temporal Series of C- and L-Band SAR Data for Soil Moisture Retrieval Over Agricultural Crops. *IEEE J. Sel. Top. Appl. Earth Obs. Remote Sens.* **2011**, *4*, 439–450. [CrossRef]
38. Balachandar Gani, N.; Periasamy, S. Synthetic Surface Roughness Using Eigen-Space Transformation Approach for Improved Surface Soil Moisture Retrieval from C-Band SAR Data. *Remote Sens.* **2026**, *18*, 2455. [CrossRef]

Disclaimer/Publisher's Note: The statements, opinions and data contained in all publications are solely those of the individual author(s) and contributor(s) and not of MDPI and/or the editor(s). MDPI and/or the editor(s) disclaim responsibility for any injury to people or property resulting from any ideas, methods, instructions or products referred to in the content.